Check for updates

JGR Oceans

RESEARCH ARTICLE
10.1029/2021JC018001

Can the Surface Quasi-Geostrophic (SQG) Theory Explain Upper Ocean Dynamics in the South Atlantic?

Mariana Miracca-Lage[1,2], Cristina González-Haro[3,4], Dante Campagnoli Napolitano[5], Jordi Isern-Fontanet[3,4], and Paulo Simionatto Polito[1]

[1]Instituto Oceanográfico da Universidade de São Paulo, São Paulo, Brazil, [2]Now at Helmholtz–Zentrum Hereon, Geesthacht, Germany, [3]Institut de Ciències del Mar, Barcelona, Spain, [4]Barcelona Expert Centre in Remote Sensing, Barcelona, Spain, [5]Laboratoire d'Etudes en Géophysique et Océanographie Spatiales, Université de Toulouse, CNES, CNRS, IRD, UT3, Toulouse, France

Key Points:

- The surface solution dominates the total stream function in winter. It has a small yet significant contribution in summer
- The surface quasi-geostrophic (SQG) and isQG methods depend more on the seasonality of the mixed-layer depth than on the content of eddy kinetic energy
- The isQG reconstruction on the South Atlantic can reproduce mesoscale motions at depths above 500 m with a threshold of 0.5 correlation

Correspondence to:

M. Miracca-Lage,
mariana.lage@alumni.usp.br;
mariana.lage@hereon.de

Citation:

Miracca-Lage, M., González-Haro, C., Napolitano, D. C., Isern-Fontanet, J., & Polito, P. S. (2022). Can the surface quasi-geostrophic (SQG) theory explain upper ocean dynamics in the South Atlantic? *Journal of Geophysical Research: Oceans*, *127*, e2021JC018001. https://doi.org/10.1029/2021JC018001

Received 14 SEP 2021
Accepted 28 DEC 2021

© 2022. American Geophysical Union. All Rights Reserved.

Abstract Satellite altimeters provide quasi-global measurements of sea surface height, and from those the vertically integrated geostrophic velocity can be directly estimated, but not its vertical structure. This study discusses whether the mesoscale (30–400 km) dynamics of three regions in the South Atlantic can be described by the surface quasi-geostrophic (SQG) theory, both at the surface and in depth, using outputs from an ocean general circulation model. At these scales, the model surface eddy kinetic energy (EKE) spectra show slopes close to $k^{-5/3}$ (k^{-3}) in winter (summer), characterizing the SQG and quasi-geostrophic (QG) turbulence regimes. We use surface density and temperature to (a) reconstruct the stream function under the SQG theory, (b) assess its capability of reproducing mesoscale motions, and (c) identify the main parameters that improve such reconstruction. For mixed layers shallower than 100 m, the changes in the mixed-layer depth contributes nine times more to the surface SQG reconstruction than the EKE, indicating the strong connection between the quality of the reconstruction and the seasonality of the mixed layer. To further explore the reconstruction vertical extension, we add the barotropic and first baroclinic QG modes to the surface solution. The SQG solutions reproduce the model density and geostrophic velocities in winter, whereas in summer, the interior QG modes prevail. Together, these solutions can improve surface correlations (>0.98) and can depict spatial patterns of mesoscale structures in both the horizontal and vertical domains. Improved spatial resolution from upcoming altimeter missions poses a motivating scenario to extend our findings into future observational studies.

Plain Language Summary Altimeters provide sea surface height measurements from which geostrophic velocities can be calculated. However, the measurements are strict to the ocean surface and obtaining its vertical structure is an ongoing challenge. Using outputs from an ocean general circulation model, we focus on describing the dynamics of mesoscale motions (30–400 km) in three regions of the South Atlantic under the surface-quasi-geostrophic (SQG) theory. We reconstruct the stream function taking a snapshot of density (and temperature) and assess the capability of the SQG method to correctly reproduce surface and vertical fields. Our results indicate that density may drive mesoscale dynamics under specific environmental conditions, and the role played by the seasonality of mixed-layer depth and eddy kinetic energy is discussed. To further explore the vertical reconstruction, we include the barotropic and first baroclinic quasi-geostrophic (QG) modes to the surface solution, yielding fields highly correlated (>0.98) to the model outputs. The upcoming new high-resolution altimeters poses a motivating scenario to apply the SQG method of reconstruction and extend our findings into future observational studies.

1. Introduction

Redistribution of energy across scales in the ocean is key to attain an equilibrium state (McWilliams, 2016). From forcing to dissipation, processes, and energy transfers at different wavelengths are all but comprised by the ocean energy spectrum (Ferrari & Wunsch, 2009). Spanning $\mathcal{O}(10-100)$ km, the mesoscale contains the largest percentage of the global ocean kinetic energy (KE; Fu et al., 2010), represented primarily by mesoscale eddies (Aguedjou et al., 2019). With the advent of satellite altimeters, the global large and mesoscale budgets could be estimated (e.g., Stammer, 1997; Wunsch & Stammer, 1995). Using long current meter records, Wunsch (1997) proposed that the first baroclinic mode dominates the surface KE in most of the global ocean and that the first two quasi-geostrophic (QG) modes represents most of the depth-averaged KE. In the same year, Stammer (1997) obtained the global wavenumber-frequency spectrum of sea surface height (SSH) variability from 3 years of

TOPEX/Poseidon altimetric data. The author showed that all spectra presented a plateau at long wavelengths, a power spectral density break around 400 km, and energy decreasing rates close to k^{-5}, which follows the predictions of horizontally isotropic QG turbulence (Stammer, 1997). More recently, Vergara et al. (2019) revisited the wavenumber-frequency spectra and spectral slopes from the available altimetric missions. Using along-track data, the authors identified flatter slopes (k^{-2}) in the intertropical band, slopes close to $k^{-11/3}$ at midlatitudes, and around k^{-5} in the subpolar regions, showing different dynamical regimes associated with the sea surface height signal. Wang et al. (2019) pointed out that these slopes are correlated with eddy kinetic energy (EKE), being steeper when the energy is high. Both studies found regional differences between the spectra, and Vergara et al. (2019) observed a marked seasonal variation in the spectral slopes. Due to spatial resolution, however, current altimeters only provide surface fields with resolved spatial scales around 100 km, missing the ocean's smaller scales and its vertical structure. Recent studies presented different methods to infer the interior-ocean circulation from satellites (Isern-Fontanet et al., 2008; LaCasce, 2012; LaCasce & Mahadevan, 2006; Lapeyre & Klein, 2006; Qiu et al., 2016, 2020; Wang et al., 2010).

The QG and surface-quasi-geostrophic (SQG) turbulence theories are frequently invoked to explain the energy redistribution among scales, and generally operate in wavenumber and frequency space. The QG theory explores the decomposition of a geostrophic, baroclinic flow into vertical dynamical modes, obtaining the stream function from the interior potential vorticity (PV) and the background stratification (Hoskins et al., 1985). On the one hand, the QG modes are orthogonal and form a complete set; on the other hand, the solution does not allow buoyancy anomalies at the surface. The SQG theory is a reduction of Eady's model of baroclinic instability to one boundary (Lapeyre, 2009), and surface-intensified flows are driven by buoyancy gradients. It assumes that there are no PV anomalies in the interior, and the flow is driven by density anomalies. The solutions are vertical exponential-decaying profiles intensified near the surface. According to Ponte et al. (2013), mixed-layer dynamics can be, under specific conditions, diagnosed by these solutions between $\mathbb{O}(10)$ and $\mathbb{O}(500)$ km using high-resolution SSH and sea surface temperature (SST) data.

Several studies have been conducted using different approaches of the SQG method with satellite data (e.g., González-Haro & Isern-Fontanet, 2014; Isern-Fontanet et al., 2020, 2021). Isern-Fontanet et al. (2006) reconstructed surface ocean currents using microwave radiometer SST data to complement the altimeter, exploring the property that SST can be a good proxy for buoyancy under determined circumstances. The authors showed a very robust relationship when applying the SQG method to relate SST and SSH fields, being the highest correlations at wavelengths between 100 and 300 km. This initial study was then extended to scales of the order of 10 km (Isern-Fontanet et al., 2021; Isern-Fontanet & Hascoët, 2014). With the advent of the Soil Moisture and Ocean Salinity (SMOS) mission, Isern-Fontanet et al. (2016) successfully captured the mesoscale motions on the Algerian basin by applying the SQG method of reconstruction using sea surface salinity (SSS) maps in the Mediterranean Sea. Their results demonstrate that surface salinity is key to understand the eddies in the Mediterranean and that the combination of temperature and salinity yields a better estimation of buoyancy and consequently the reconstructed velocities. From the perspective of remote sensing, the SQG method has the advantage of only requiring a single SST and/or SSS snapshot to obtain velocities (Isern-Fontanet et al., 2017).

Similarly, the SQG methodology was also applied using numerical simulations (e.g., Klein et al., 2009; Wang et al., 2013). Klein et al. (2009) aimed to diagnose vertical velocities using sea surface height data from a high-resolution numerical simulation, using a simpler version of the aforementioned method termed eSQG. The low-frequency motion, 3D fields were satisfactorily reconstructed between 20 and 400 km, indicating that this is a potential approach to obtain horizontal and vertical fluxes of tracers in the ocean. More recently, Qiu et al. (2020) reconstructed the vertical velocity and vorticity using the same eSQG approach, extending the results of Qiu et al. (2016) by using higher-resolution model outputs with tidal forcing and including unbalanced motions to the reconstruction. The authors bring the discussion to the applicability of these methods to the data from the upcoming high-resolution altimeters, and show that the reconstruction degrades beneath the mixed layer due to altimeter sampling. This happens because the errors associated with the altimeter affect more the shallow-reaching portions of the smaller scales, whereas the mesoscales can penetrate deep into the ocean interior. On the other hand, Wang et al. (2013) developed a more sophisticated SQG method to retrieve information from surface data, based on the coupling between the surface solutions from SQG and the vertical modes from the QG theory. Their results using an ocean circulation model showed that the method is successful in retrieving subsurface fields for both energetic regions (e.g., the Gulf Stream) and in the less-energetic eastern subtropics. The authors named

this method isQG, and it will be described in the following section. A different direction, devoted to improve the reconstruction of surface velocities, is the use of empirical transfer functions (González-Haro et al., 2020; González-Haro & Isern-Fontanet, 2014; Isern-Fontanet et al., 2014).

Flow reconstruction using the SQG theory has also been explored as a valuable tool to describe subsurface dynamics (e.g., Lapeyre & Klein, 2006). Using a numerical simulation, Lapeyre and Klein (2006) investigated the relationship between the surface-intensified flow (from SQG) and the traditional QG interior modes in the Antarctic Circumpolar Current, showing that SQG solutions dominate the first 500 m, and that buoyancy and interior PV were anticorrelated. This derives from the correlation between surface density and interior PV, locking the phase between SSH and buoyancy anomalies (Isern-Fontanet et al., 2006), allowing the surface stream function to be determined from one snapshot of density anomaly. However, the surface signature of SSH and density may differ, often due to the response of the mixed layer to surface heating and cooling (LaCasce & Mahadevan, 2006). Isern-Fontanet et al. (2008, 2014) showed the dependence of SQG reconstruction on the dynamics of the mixed layer on the North Atlantic Ocean and on the Mediterranean Sea, respectively, further corroborated globally by González-Haro and Isern-Fontanet (2014). Briefly, correlations tend to increase where thermal gradients, the mean wind, or the mixed-layer depth (MLD) is large. Sasaki et al. (2014) showed that there is an important seasonal cycle driven by the atmosphere which affects the SSH variability in a high-eddy-energy region on the North Atlantic. During summer, a shallow MLD imply low available potential energy, whereas in winter a deeper MLD have the opposite effect (Callies et al., 2015; Napolitano et al., 2021). In addition, the mixed layer is not horizontally homogeneous, and horizontal density gradients can modify its thickness and horizontal structures (Tandon & Garrett, 1995).

The SQG flow presents a KE spectrum with slopes following a $k^{-5/3}$ power law, and a SSH spectrum of $k^{-11/3}$ (Blumen, 1978). Le Traon et al. (2008) showed that for energetic regions such as the Gulf Stream, the SSH spectral slopes from altimetric measurements departed from the QG turbulence theory (k^{-5}), being closer to the ones predicted by SQG, and consequently suggesting that the SQG framework would better represent upper-ocean dynamics in these regions. Later, using a high-resolution numerical simulation, Sasaki and Klein (2012) showed SSH spectral slopes of k^{-4} in both low- and high-energy regions—which is also close to SQG predictions—and attributed the flatter slopes found by Le Traon et al. (2008) to altimetry noise. Besides, the altimeter's flatter slopes were also attributed to internal tides and the shift of the inertial sub-range to smaller scales (Richman et al., 2012). Recently, Vergara et al. (2019) showed that altimeter's SSH spectral slopes vary seasonally and geographically. They found that western boundary regions with energetic mesoscale motions present slopes between k^{-4} and k^{-5}, and flatter slopes in less energetic regions.

In the present study, we use outputs from a global numerical model in three distinct regions of the South Atlantic. We ask: can the SQG theory be used to explain the mesoscale upper-ocean dynamics in these regions? To address this question, we (a) investigate how local dynamics and seasonality affect the efficiency of the surface-flow reconstruction and (b) evaluate how these spatio-temporal variations—added to the contribution of the interior PV—may impact the reconstruction of the vertical structure. Next, Section 2 provides the theoretical background for the surface and vertical reconstructions. In Section 3, we show the characterization of each area in terms of KE wavenumber spectra and spectral slopes. Finally, we present our discussion of the surface stream function reconstruction (Section 4), and the solutions for the vertical structure in Section 5.

2. Theoretical Background

Assuming that the flow is quasi geostrophic and on the f-plane, dynamics are determined by the conservation of potential vorticity. Given the invertible relation (Hoskins et al., 1985), we obtain the geostrophic stream function (ψ) from the PV (q)

$$q(x,y,z,t) = \nabla^2\psi + \frac{\partial}{\partial z}\left(\frac{f_0^2}{N^2}\frac{\partial\psi}{\partial z}\right), \tag{1}$$

where f_0 is the Coriolis parameter, $N(z)$ is the Brunt-Väisälä frequency, and $\nabla \overset{\text{def}}{=} \left(\frac{\partial}{\partial x}, \frac{\partial}{\partial y}\right)$. As vertical boundary conditions, we enforce:

$$\begin{cases} f_0 \dfrac{\partial \psi}{\partial z} = b_s \quad \text{at} \quad z = 0\,, \quad \text{and} \\ f_0 \dfrac{\partial \psi}{\partial z} = 0 \quad \text{at} \quad z = -H\,. \end{cases}, \tag{2}$$

In Equation 2, $b_s(x, y, t) \overset{\text{def}}{=} -g(\rho - \rho_0)/\rho_0$ is the surface buoyancy, where $\rho(x, y, t)$ is the surface density, $\rho_0 = 1{,}025$ kg m^{-3} is a reference density, and H is the depth of the bottom boundary (5,000 m in this study).

Setting different values for the surface boundary condition in Equation 2 yields two solutions for Equation 1. Removing the surface buoyancy ($b_s = 0$) and allowing for PV anomalies in the ocean interior ($q \neq 0$) leads to the QG solution, represented by the interior stream function ψ_{int}. The second solution comes from the surface-quasi-geostrophic theory (SQG; Held et al., 1995); in this case, advection of buoyancy anomalies ($b_s \neq 0$) leads to the stirring of buoyancy contours and the development of horizontal fronts (Lapeyre & Klein, 2006). This SQG flow (herein called ψ_{sqg}) is associated with frontogenesis without ageostrophic movements, and, contrary to ψ_{int}, assumes no interior PV anomalies ($q = 0$). Due to the linearity of the system of Equations 1 and 2, its solution accounts for both the SQG and QG contributions, thus

$$\psi = \psi_{sqg} + \psi_{int}\,. \tag{3}$$

According to LaCasce (2012), to obtain ψ_{sqg} we expand the surface information downward through a vertical transfer function χ by solving

$$\frac{\partial}{\partial z}\left(\frac{f_0^2}{N^2}\frac{\partial \chi}{\partial z}\right) - K^2\chi = 0\,, \tag{4}$$

where $K = |\mathbf{k}|$ is the magnitude of the wavenumber vector $\mathbf{k} = (k_x, k_y)$. Using a regionally averaged, depth-dependent Brunt-Väisälä profile $N(z)$ from a numerical model, we numerically solve Equation 4 for χ in the Fourier domain with the boundary conditions:

$$\begin{cases} \dfrac{\partial \chi}{\partial z} = 1 \quad \text{at} \quad z = 0\,, \quad \text{and} \\ \dfrac{\partial \chi}{\partial z} = 0 \quad \text{at} \quad z = -H\,. \end{cases}, \tag{5}$$

With the exponential-like transfer function χ, surface-buoyancy information b_s is transferred through the water column, yielding, for each time step t:

$$\widehat{\psi}_{sqg}(\mathbf{k}, z, t) = \widehat{b}_s(\mathbf{k}, t)\ \ \chi(K, z)\,. \tag{6}$$

We thus obtain the stream function $\widehat{\psi}_{sqg}$ (the caret denotes the horizontal Fourier transform) for a double periodic domain with mirror symmetry (e.g., Isern-Fontanet et al., 2006).

The ψ_{sqg} approximation derived from Equations 1 to 5 performs best at the surface, because buoyancy anomalies are present at the surface and vanish toward the bottom. Although Equation 6 alone can represent well the dynamics in the top 500 m in some regions, it may lack crucial information in others (e.g., Isern-Fontanet et al., 2008). This happens because surface density and sea surface height are not always phase-locked (González-Haro & Isern-Fontanet, 2014), which may result from surface heating and cooling significantly altering the surface expression of the buoyancy (LaCasce & Mahadevan, 2006). Moreover, the assumption that PV in the interior is zero may not always be valid, which would require extending the field reconstruction to include both ψ_{sqg} and ψ_{int}.

To overcome these limitations, Wang et al. (2013) first proposed the isQG method of reconstruction, which combines the surface solution (Equation 6) with QG vertical modes; the authors numerically solved the SQG stream function for non-constant stratification and included the barotropic and first baroclinic modes, given additional boundary conditions. In brief, the interior solution ψ_{int} at the surface is projected into the vertical dynamical modes, using the QG modal decomposition

$$\widehat{\psi}_{int}(\mathbf{k}, z, t) = \sum_{j=0}^{1} A_j(\mathbf{k}, t) F_j(z)\,, \tag{7}$$

in which we obtain the QG modes vertical structures F_j using a regionally averaged N^2 from a numerical simulation. Then, the modal amplitudes A_j can be calculated from Equation 7, given that ψ_{int} is retrieved at the surface by removing the contribution of ψ_{sqg} from the total stream function ψ (see Equation 3), yielding, in the Fourier domain

$$\widehat{\psi}(\mathbf{k},0) = \frac{g}{f_0}\widehat{\eta}(\mathbf{k}) = \widehat{\psi}_{sqg}(\mathbf{k},0) + \widehat{\psi}_{int}(\mathbf{k},0)\,, \tag{8}$$

where $\widehat{\eta}$ is the Fourier transform of the surface elevation and $g = 9.8$ m s^{-2} is the acceleration due to gravity. At the bottom, pressure vanishes in both the SQG and QG solutions, thus

$$\widehat{\psi}_{sqg}(\mathbf{k},-H) + \widehat{\psi}_{int}(\mathbf{k},-H) = 0\,. \tag{9}$$

For further details on the isGQ method, we refer the reader to Wang et al. (2013).

The SQG and isQG frameworks are used to determine the influence of surface boundary on the dynamics of the upper ocean. The advantage of invoking the SQG theory is precisely the projection of surface information to depth through an exponential-like transfer function. However, as mentioned above, there are limitations to which extent SQG is effective. Next, we narrow down spatio-temporal conditions where SQG poses a good representation—or not—of the mesoscale circulation.

3. The Surface Kinetic Energy Spectra in the South Atlantic

Testing the ability of the SQG and isQG reconstructions to fully represent surface and interior motions requires high-resolution data in time and space. Here, we use the Hybrid Coordinate Ocean Model-Navy Coupled Ocean Data Assimilation (HYCOM-NCODA, henceforth HYCOM) reanalysis, which assimilates in situ data from Argo, XBTs, moored buoys, and satellite data (SST, SSH) using the NCODA system (Chassignet et al., 2009; Cummings, 2005). HYCOM reanalyzes have shown consistent results in the South Atlantic (e.g., Lima et al., 2016; Magalhães et al., 2017; Simoes-Sousa et al., 2021; Thoppil et al., 2011; Wang et al., 2013). The reanalysis used in this study (Experiment 19.1) provides four-dimensional sea-estate estimates at time 00Z, with spatial resolution $\Delta x = 0.08° \simeq 10$ km and 40 vertical z-levels spanning 0–5,000 m. The surface forcing includes hourly wind stress, precipitation and heat fluxes from the National Centers for Environmental Prediction (NCEP) Climate Forecast System Reanalysis (CFCR). Next, we apply the SQG method on 5 years (2008–2012) of reanalysis outputs—SSH, salinity, and temperature—to reconstruct the geostrophic stream function over three regions of the South Atlantic with distinct dynamical regimes.

3.1. EKE and Mesoscale Motions

We selected three regions with distinct regional mean surface EKE (Figure 1a). All regions have $10° \times 10°$, large enough to capture the mesoscale, which we here define as motions with horizontal scales spanning 30–400 km. Within our regions, the first-baroclinic Rossby deformation radius is $\mathbb{O}(10)$ km (Houry et al., 1987). To separate such regions, we applied a Lanczos filter to isolate the aforementioned mesoscale horizontal scales from the model total surface velocities, $(u, v) = (\overline{u}, \overline{v}) + (\tilde{u}, \tilde{v})$, where the tilde denotes our mesoscale eddy field that defines the EKE and the eddy vorticity:

$$\begin{aligned} \text{EKE} &\overset{\text{def}}{=} 0.5(\tilde{u}^2 + \tilde{v}^2)\,, \\ \zeta &\overset{\text{def}}{=} \frac{\partial \tilde{v}}{\partial x} - \frac{\partial \tilde{u}}{\partial y}\,. \end{aligned} \tag{10}$$

In the subtropical South Atlantic, the three selected regions, namely the Brazil Current (BC), Brazil-Malvinas Confluence (BMC), and the Agulhas leakage (Ag) regions, are highlighted in Figure 1. The BC flows poleward, flanking the Brazilian continental shelf (Peterson & Stramma, 1991; Silveira et al., 1994; Soutelino et al., 2011) up to 38°S–40°S, where it converges with the Malvinas Current to form the BMC, known to be one of the most energetic regions in the world (e.g.,: Legeckis & Gordon, 1982). Oliveira et al. (2009) analyzed the energetics of the BC in the western South Atlantic using 13 years of surface drifters. The authors showed that, in general, the mean flow of the BC have larger values of KE in comparison with the energy of perturbations, but when the current

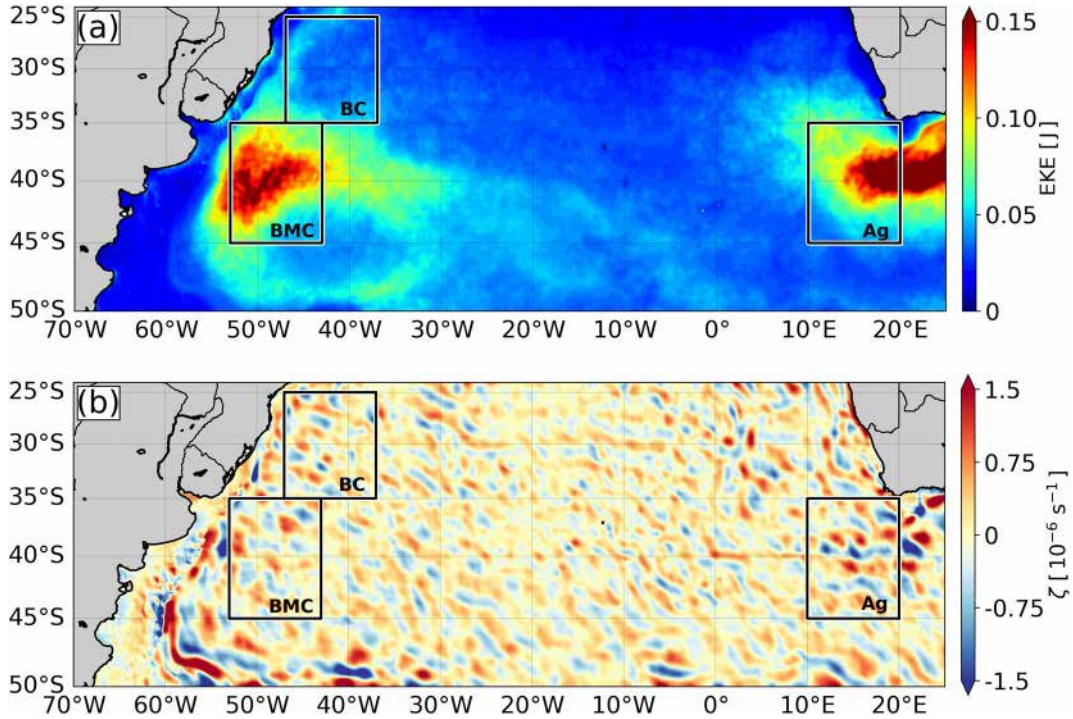

Figure 1. (a) Mean eddy kinetic energy (EKE) and (b) eddy vorticity for the South Atlantic from January 2008 to December 2012 estimated from HYCOM surface velocity. Boxes delimits the study areas, namely BC, BMC and Ag regions.

meets the Malvinas Current at the BMC, the EKE has larger or comparable values to the mean KE, reflecting into high mesoscale activity in the area. More recently, Magalhães et al. (2017) used HYCOM reanalysis outputs to investigate energy transfers in 19 transects between 20°S and 36°S. They showed that EKE increases southward, with larger values in the offshore portion of the BC, expanding previous results of Silveira et al. (2004, 2008) on the baroclinicity of the current system. A considerable part of the EKE at these latitudes is due to the presence of first-mode baroclinic Rossby waves. Polito and Liu (2003) estimated that from 25°S to 35°S, 35%–50% of the SSH variance is due to Rossby waves with periods centered between 6 and 24 months. Oliveira and Polito (2013) showed that, at these latitudes, the Rossby wave related SSH anomalies are tightly correlated with those in the SST, with a decorrelation scale of $\mathbb{O}(10^3)$ km.

The most energetic of our regions is the Agulhas Current leakage in the eastern South Atlantic, a highly energetic region with intense mesoscale activity (Gordon & Haxby, 1990; Pegliasco et al., 2015; Richardson, 2007). Gordon and Haxby (1990) observed Agulhas rings entering the South Atlantic with a sequence of the Geosat altimeter and CTD data. These eddies carry trapped warm waters from the Indian Ocean, that are smoothly converted into South Atlantic waters. Richardson (2007) analyzed the EKE from drifters, showing that cyclones and anticyclones in the vicinity of the Agulhas retroflection were the most energetic in the southeastern Cape Basin. Besides the well-known Agulhas eddies, Pegliasco et al. (2015) reported several eddies generated at the South Atlantic eastern boundary due to coastal dynamics, which contribute to the high EKE in the region. Between 35°S and 45°S, the variance explained by first-mode baroclinic Rossby waves reaches a local minimum of ~25% at 40°S due to the vigorous eddy activity at the BMC and Ag regions (Polito & Liu, 2003). In this latitude range, only Rossby waves with periods centered above 12 months are permitted by the dynamics. Furthermore, according to Oliveira and Polito (2013) the decorrelation between SSH and SST due to Rossby waves at 35.5°S falls to $\mathbb{O}(10^2)$ km, clearly showing the dominance of mesoscale eddies in both fields. Altimetric observations show a positive tendency for energetic eddies in the Ag region; in the BMC, this tendency is negative (Polito et al., 2008).

The three selected regions differ in their content of EKE and associated vorticity (Figures 1a and 1b, respectively), being the BC the least energetic region. The proportion between mesoscale eddies and Rossby waves associated with the observed EKE differs, with the BMC and Ag regions dominated by eddies while at the northernmost box Rossby waves play a relatively larger role. In the BC case, a significant amount of EKE is associated

with the mesoscale activity due to the meandering of the BC, for example, at the Rio Grande cone region (Brum et al., 2017). The BMC is the second most energetic region, with its energy drawn from the interaction between the confluent jets (e.g., Garzoli & Garraffo, 1989), followed by the Ag, where the Agulhas rings formation drive the highest EKE in the South Atlantic (e.g., Peterson & Stramma, 1991). At all regions, values of eddy vorticity follows the spatial patterns of EKE, which confirms that the amount of EKE is consequence of mesoscale activity. Moreover, Rossby-number estimates $Ro = \mathbb{U}/f\mathbb{L}$ yield order $\mathbb{O}(10^{-2})$ for all three areas, suggesting that mesoscale activity is dominant and ageostrophic processes are weak.

3.2. Kinetic Energy Spectral Signature: Slopes

In the spectral domain, the slopes show how the KE is distributed through wavenumbers (or wavelengths) and can be used to determine the predominant dynamics of the flow. The dynamics of mesoscale eddies generated by horizontal QG PV gradients in the ocean interior follow the Phillips regime (Phillips, 1954). This particular energy spectrum is characterized by a slope of k^{-3}, implying that the energy is mostly within the larger scales. Smaller-scales would have little contribution on the mesoscale eddies energy budget in this case. In contrast, more recent studies (Le Traon et al., 2008; Richman et al., 2012; Xu & Fu, 2012) reported spectral slopes flatter than the k^{-3} predicted by the QG-turbulence theory, suggesting that the smaller scales can impact the larger scales. In this case, the turbulent dynamics follows the Charney regime, and instabilities derive from the interaction between the surface PV and the interior PV, the former being driven by surface density anomalies (Blumen, 1978; Held et al., 1995; Lapeyre & Klein, 2006). The energy would then present a flatter ($\sim k^{-2}$) slope, with the smaller-scale structures [$<\mathbb{O}(10^2)$ km] associated with frontogenesis due to the mesoscale eddies. These smaller scale features enhance the KE from eddies, a characteristic of the inverse energy cascade. Thus, computing the spectral slopes of different surface variables (e.g., SSH, KE) indicates whether the surface flow follows the predictions of the simplified ocean-dynamics models, like the aforementioned QG or SQG. The SQG theory, associated with the Charney regime, predicts a KE slope $k^{-5/3}$ for its wavenumber spectrum, while the traditional QG-turbulence theory, follows a k^{-3} power law.

For daily snapshots of KE in each $10° \times 10°$ area, we removed the temporal and spatial mean and estimated the isotropic power spectral density using a 2D discrete fast Fourier transform with a Hanning tapering window. The resultant 2D spectrum is binned and averaged in the azimuthal direction. The spectral slopes were calculated with a linear least-squares regression of the resulting power spectral density in the mesoscale band (30–400 km). Figure 2 shows the temporal evolution of the spectral slopes for each area, as well as the KE wavenumber spectrum for a day in winter. Essentially, daily spectral slopes in all areas ranged between values estimated by the SQG ($k^{-5/3}$) and the QG (k^{-3}) theories. The BC region (Figure 2a) presented the steepest mean spectral slope (-2.8 ± 0.09), closer to QG. The BMC (Figure 2b) and Ag (Figure 2c), our most energetic regions, presented an average slope between QG and SQG predictions, with -2.7 ± 0.09 for BMC and -2.6 ± 0.1 for Ag. Richman et al. (2012) used HYCOM outputs to estimate the spectral slopes for the KE in the Pacific Ocean. As with our results, their slopes lied between the QG and SQG predictions, particularly in regions of high eddy kinetic regions and weak tides.

For all areas in Figure 2, a seasonal variation of the spectral slopes can be readily depicted. Steeper slopes (i.e., more negative) occur during summer (DJF in the Southern Hemisphere), while flatter slopes appear during winter (JJA). Slopes peak around early spring (September; $\sim k^{-2}$) and reach QG-driven values of $\sim k^{-3}$ around February. The peaks can result from the influence of unbalanced motions, as reported by Rocha, Gille, et al. (2016) from the analysis of 13 years of ADCP data in the Drake Passage. The departure from the QG regime observed during winter and early spring is consistent with reports of increased submesoscale activity in numerical simulations at this period (e.g., Callies et al., 2015; Napolitano et al., 2021; Rocha, Chereskin, et al., 2016; Sasaki et al., 2014), being also detected in altimetry data (Dufau et al., 2016; Vergara et al., 2019) and by in situ observations (Callies et al., 2015). In winter, when the mixed layer is deep and stratification is weak, there is more available potential energy and the EKE produced by mixed-layer instabilities is higher than in summer, when the opposite occurs (Callies et al., 2015). The seasonal cycle of the mixed layer thus affect the KE and consequently the spectral slopes, and it may be altered (not exclusively) by the presence of submesoscale instabilities (e.g., Sasaki et al., 2014), inertia-gravity waves (e.g., Rocha, Chereskin, et al., 2016), and flow-topography interactions (e.g., Napolitano et al., 2021). For more details in the seasonality of KE spectra, see Uchida et al. (2017).

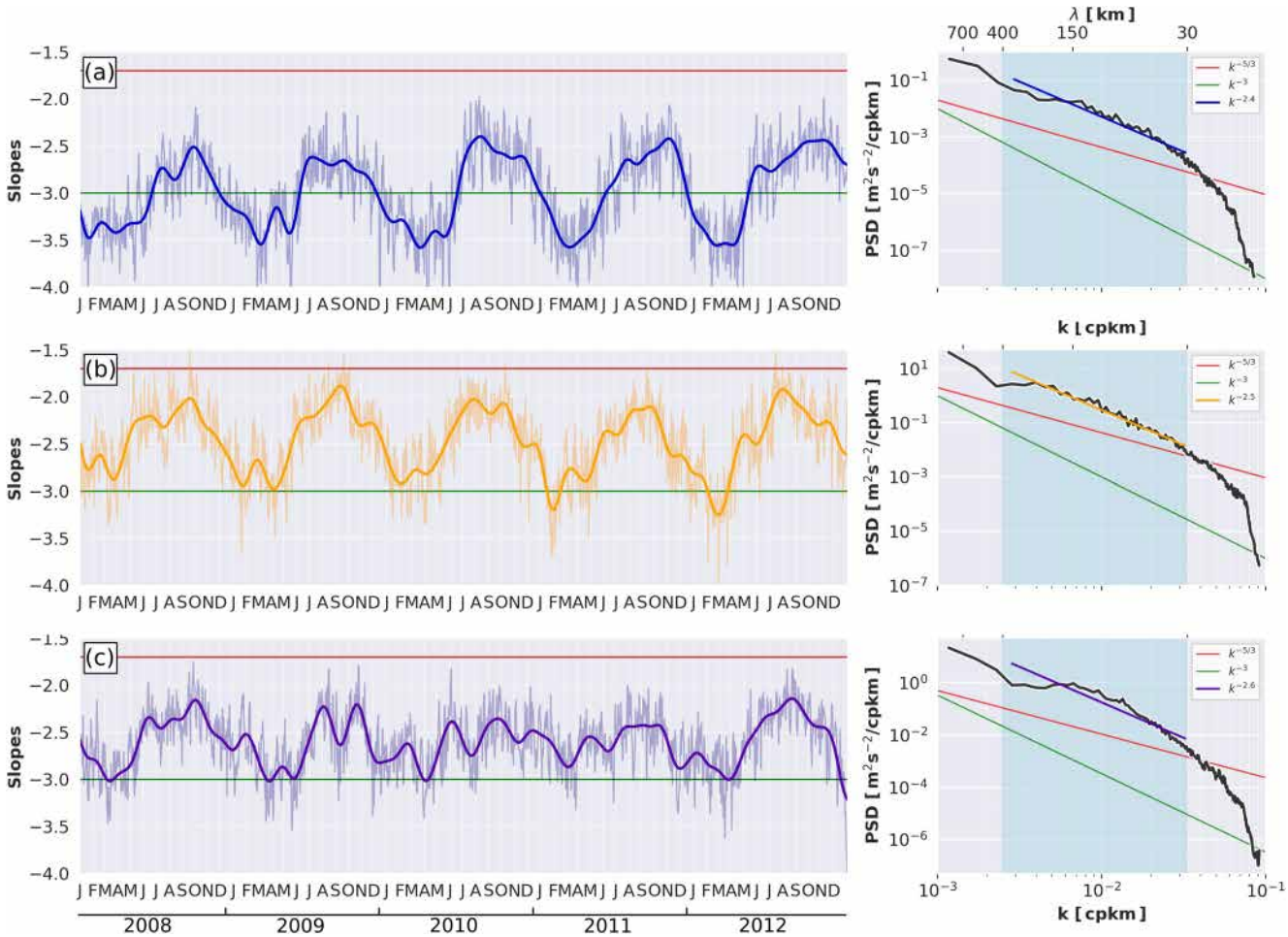

Figure 2. (Left) Daily temporal variation of kinetic energy (KE) spectral slopes (colored lines) and monthly averaged (colored smooth solid lines). (Right) KE spectrum (black line) for (a) BC (19 July 2012), (b) BMC (21 July 2008), and (c) Ag (24 July 2011) regions. The blue hatched area corresponds to the mesoscale range where the linear regression was performed. Slopes for SQG (red line; $k^{-5/3}$) and QG (green line; k^{-3}) theories are plotted as a reference. PSD, power spectral density.

With KE slopes between QG and SQG, the flatter slopes in winter (Figure 2) associated with the energy contained in the mixed layer suggest that density gradients may be important to the region's surface variability. It is worth mentioning that our HYCOM experiment does not include tidal forcing and its horizontal resolution cannot resolve the submesoscale; yet, high-frequency wind forcing generates super-inertial energy, which seems to have a large contribution to the energy of mesoscale processes, given the seasonal fluctuations of the spectral slopes. In this scenario, SQG stages an alternative to a rigid-lid QG model for the reconstruction of surface fields.

4. The Surface Reconstruction: SQG Solutions

The strong seasonal dependence on the spectral slopes reported in the previous section motivated us to further investigate the limitations of different SQG solutions and their applicability for the reconstruction of the flow. We start analyzing the relationship between the performance of the SQG reconstruction and the seasonality of mixed-layer dynamics, as previously reported by, for example, Isern-Fontanet et al. (2008) and González-Haro and Isern-Fontanet (2014).

4.1. Seasonality of the SQG Reconstruction

To assess the ability of SQG to reconstruct surface fields, we first calculated the SQG surface stream function (ψ_{sqg}) from Equation 6 for daily HYCOM snapshots under two different approaches: we obtained the surface

buoyancy using (a) density and (b) SST anomalies (see González-Haro & Isern-Fontanet, 2014; Isern-Fontanet et al., 2008 for details). Second, we applied a Lanczos filter to retain mesoscale wavelengths between 30 and 400 km. For the MLD, we followed the threshold criteria (see de Boyer Montégut et al., 2004 and references therein). We defined the MLD as the shallowest depth at which the density σ_0 and temperature differ by 0.1 kg m^{-3} and 0.2°C from surface values, respectively, and confirmed the criteria with visual inspection of the profiles. We averaged the MLD derived from σ_0 and SST, and the resulting two-dimensional MLD was spatially averaged, yielding one daily averaged MLD for each of our study areas. To evaluate if the SQG reconstruction alone represents the surface flow, we analyze the statistically significant spatial correlations (i.e., with $p < 0.05$) between ψ_{sqg} and the surface model stream function $\psi = g\eta/f_0$.

Density anomaly presents a natural choice of variable for the ψ_{sqg} reconstruction. Yet there were several studies (González-Haro & Isern-Fontanet, 2014; Isern-Fontanet et al., 2006, 2020; LaCasce & Mahadevan, 2006; Turiel et al., 2008) that used SST as a proxy for surface buoyancy, because it can be measured remotely from satellite sensors. One key assumption for using SST or density for the SQG reconstruction is that these properties are in phase with SSH contours (e.g., Lapeyre & Klein, 2006), which allows the reconstruction from a SST or density snapshot. However, this assumption does not hold everywhere, nor it does throughout the year (González-Haro & Isern-Fontanet, 2014; Isern-Fontanet et al., 2014; Lapeyre, 2009).

The time series of the spatial correlation between the surface geostrophic stream function from the model ψ and ψ_{sqg} estimated from density (blue) and temperature (red) anomalies is shown in Figure 3. In general, both reconstructions performed similarly throughout their time series, with higher correlations in winter and lower correlations in summer, as also reported by Isern-Fontanet et al. (2006), González-Haro and Isern-Fontanet (2014), and Liu et al. (2014). This suggests that both density and temperature are good proxies for the SSH, and both resemble the density below the mixed layer, with a minimum phase shift between σ_0 (or SST) and the SSH (Isern-Fontanet et al., 2008, 2014). Nevertheless, differences among areas are readily identified. The BC region presented the lowest correlation values (Figure 3a) between ψ and ψ_{sqg} of all areas. For this region, the reconstructions using SST and density are somewhat not in phase, even though both reconstructions yield similar mean correlations, with 0.39 and 0.37 for temperature and density reconstructions, respectively. While the overall higher values are linked to the density reconstruction in winter, the SST-based reconstruction performs better than σ_0 in summer. The density reconstruction cycles in accordance with variations of the mixed layer (Figure 3a), with a 0.7 correlation, whereas the ψ–ψ_{sqg} correlation derived from SST presents a correlation of 0.15 with the mixed layer cycle, indicating that, *using density*, a deep mixed layer favors the flow reconstruction. Our results corroborate González-Haro and Isern-Fontanet (2014), which expected low correlation between ψ and ψ_{sqg} at low latitudes and overall at lower EKE regions.

The BMC (Figure 3b) and Ag (Figure 3c) regions presented larger daily correlations, ranging on average from 0.6–0.2 for the BMC and 0.8–0.4 for the Ag in winter–summer, respectively. At the BMC region, winter correlations using either SST or σ_0 are similar, with density presenting the highest peaks by a small margin. During summer, however, there is a mismatch between the reconstructions, and temperature gives the best estimation of the surface stream function (Figure 3b). These summertime values carry the ψ–ψ_{sqg} correlations using temperature to, on average, present higher values (0.61) in respect to the ψ–ψ_{sqg} correlations using density (0.47). Once again, the correlation with the mixed layer is clearer in the density reconstructions, implying that SST is less sensitive to the mixed layer seasonal cycle and SST variations may on average mirror the variations from density below the mixed layer, as discussed by Isern-Fontanet et al. (2008). Isern-Fontanet et al. (2008) also argued that the depth of the mixed layer seems to be a better indicator of the quality of the reconstruction, which we confirmed particularly for the density reconstructions. Lastly, in the Ag region the discrepancies between the σ_0 and SST reconstructions are minimum (correlations of 0.55 and 0.53, respectively), with density performing best nearly through all the series. The mixed-layer cycle is also the weakest, with a standard deviation of 30 m in the MLD, compared to 35 m for the BC and 39 m for the BMC, which may have contributed to the similar correlations.

To further investigate the relationship between the different SQG reconstructions and the MLD, we display on Figure 4 the ψ and ψ_{sqg} correlations with an increasing MLD. González-Haro and Isern-Fontanet (2014) analyzed the dependence on the SQG reconstruction on three parameters, namely the standard deviation of the thermal gradient, the root mean square of the MLD, and the mean wind. The authors concluded that the reconstruction is better when the thermal gradient is large, when the mixed layer is deep, and when the wind is strong; nevertheless, all parameters presented similar geographical patterns and similar correlations between the original field

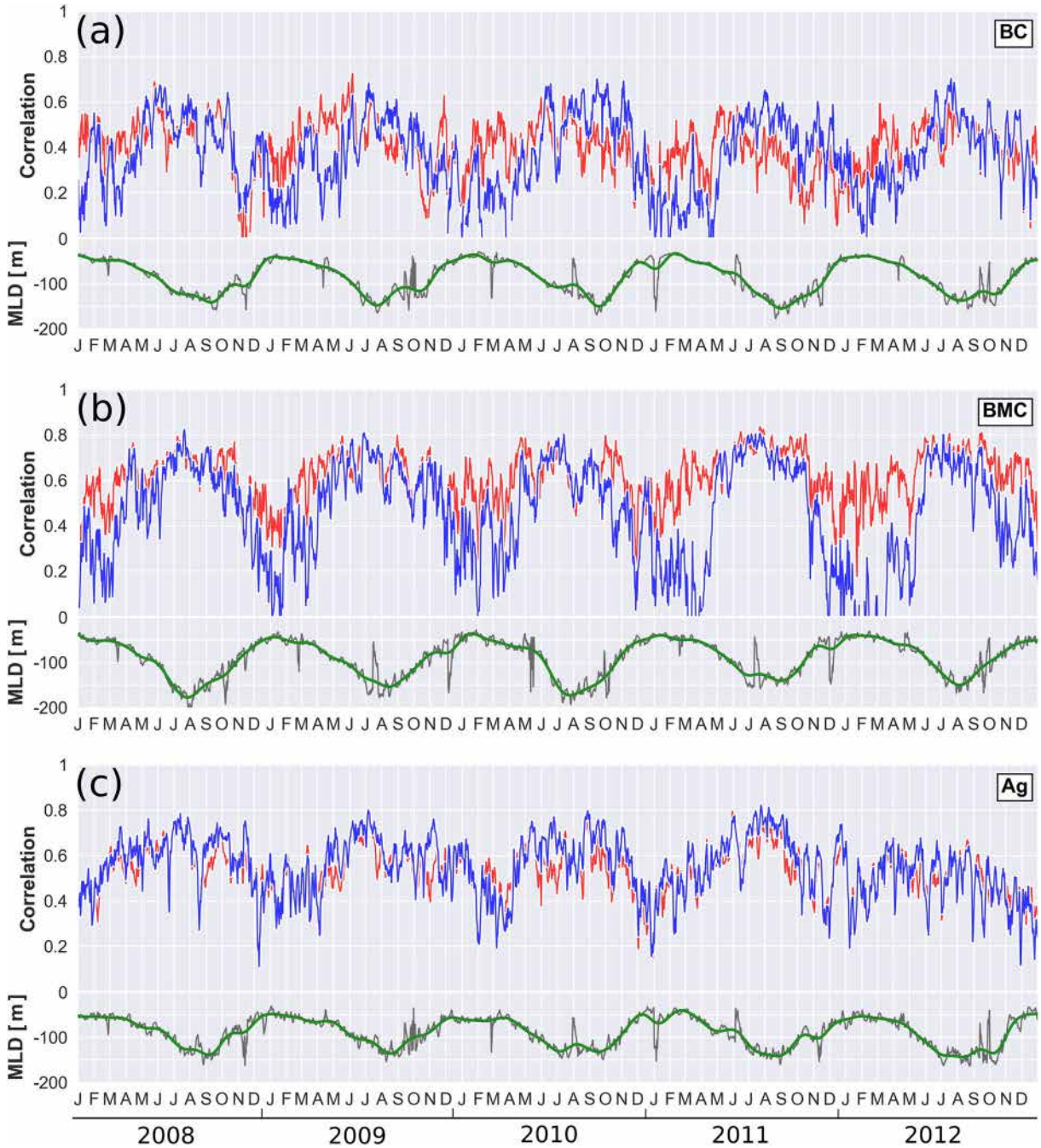

Figure 3. (Top) Spatial correlations between the geostrophic stream functions from HYCOM (ψ) and from our reconstruction (ψ_{sqg}) using buoyancy (blue) and sea surface temperature (red) anomalies, from January 2008 to December 2012, for the (a) BC, (b) BMC, and (c) Ag regions. Only correlations with a significance level of 95% were plotted. (Bottom) Daily (gray line) and monthly averaged (green line) mixed-layer depth.

and the reconstructed one. In Figure 4, the dependence on the MLD is readily depicted for density: the deeper the mixed layer, the larger the correlation. Conversely, this relation is not obvious for SST, particularly for the BC region (Figure 4a). There, correlations barely change throughout the year. At the BMC (Figure 4b), the pattern is similar to density, with correlations larger for a deep mixed layer. This increment is nearly constant for SST, but skyrockets for density at MLD < 100 m. The linear trend is also noted in Ag, with minimum mean correlations around 0.4 increasing to about 0.6 as the MLD gets deeper. In this region, we observe no remarkable difference between density and SST.

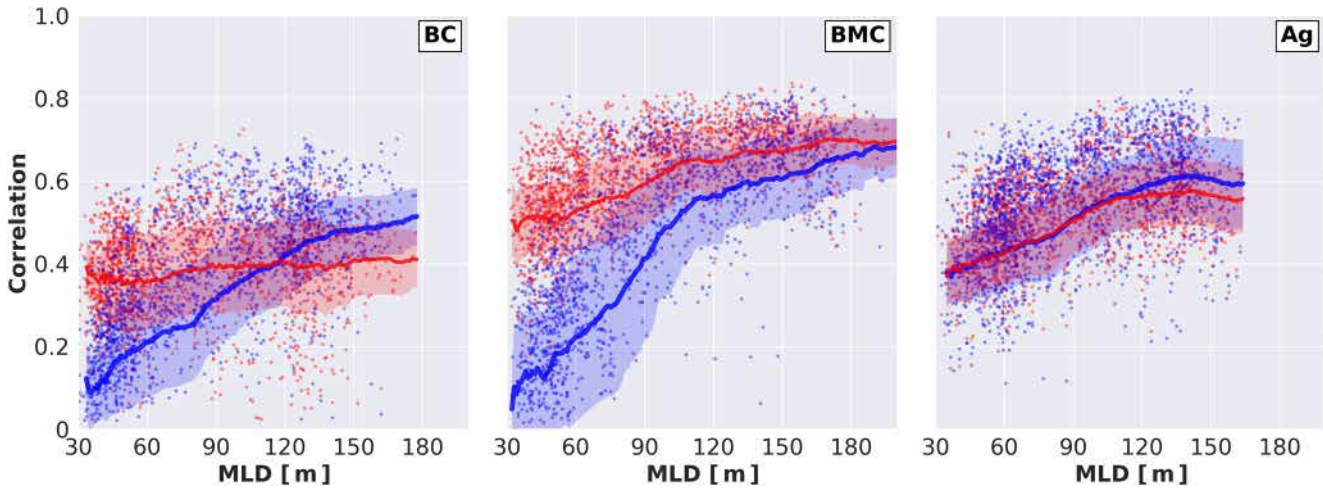

Figure 4. Scatterplot of the daily correlations between ψ and ψ_{sqg} from buoyancy (blue) and sea surface temperature (red) and the mixed-layer depth, from January 2008 to December 2012. Solid lines and shaded area represent the mean and one standard deviation, respectively.

Although larger correlations between ψ and ψ_{sqg} may appear in the SQG reconstruction based on SST, the largest correlations during winter also occur with the density based reconstruction, with 0.70, 0.82, and 0.83 for the BC, BMC, and Ag, respectively. Moreover, the correlation values of the density-based reconstruction depends on the mixed-layer cycle, suggesting that there is indeed preferential regions and seasons to adequately apply the SQG reconstruction. In general, mean correlations using density are higher than SST in winter and spring, but lower in summer and fall. In Isern-Fontanet et al. (2016), the authors used SSS observations from SMOS in addition to satellite SST, improving the surface stream function retrieval, especially the sign of vorticity (e.g., Isern-Fontanet et al., 2016). The foundation of the SQG theory is density, and as we focus on meso-to-submesoscale variability, direct measurements do not provide the necessary spatial and temporal resolution. Thus, in the following sections we take advantage from HYCOM's surface density fields and use only density-based reconstructions.

4.2. Spatial Patterns of Sea Surface Height

To evaluate our SQG reconstruction, we selected the day of the largest correlations between ψ and ψ_{sqg} for each area and present the surface fields in terms of SSH (η). We recall from Equation 8 that, at the surface, $\eta = \psi f_0/g$. We calculated η from the total stream function ψ, η_{sqg} from the SQG solution ψ_{sqg}, and η_{int} from the residual stream function ψ_{int} (the two terms summed up yield at least 0.98 ψ–ψ_{sqg} correlation). For the highest correlations in winter, Figure 5 breaks down the model's SSH (η) into the surface (η_{sqg}) and interior contributions (η_{int}), and demonstrates the potential of employing the SQG theory in the reconstruction of surface fields. The resemblance between η and η_{sqg} in all areas shows that SQG is capable of reproducing the spatial patterns of the model, which is reflected by high correlations between η and η_{sqg}, namely 0.70 for the BC (Figures 5a and 5b), 0.82 for the BMC (Figures 5d and 5e), and 0.83 for the Ag (Figures 5g and 5h). The representation of the anti-cyclonic features around 40°S–46°W at the BMC (Figures 5d and 5e) stands out, as well as the sequence of elevations and depressions in the northeastern portion of Ag. Nevertheless, some discrepancies can be noted, which accounts approximately for the 17%–30% mismatch between η and η_{sqg}. These discrepancies appear as regions well represented by η_{int}, such as the cyclone centered at 38°S–51°W in Figures 5d and 5f and the anticyclone close to 34°S–42°W in Figures 5a and 5c. For the reconstruction during summer (not shown), correlations are lower, and the patterns between η and η_{sqg} are less correspondent, although the SQG reconstruction can still depict some features. For the SQG velocities and vorticity, results were similar, with slightly lower correlations. We recall that high correlations between ψ and ψ_{sqg}, as well as similar spatial patterns and magnitudes occur especially during winter and early spring, and seasonality drives important changes in the SQG efficiency.

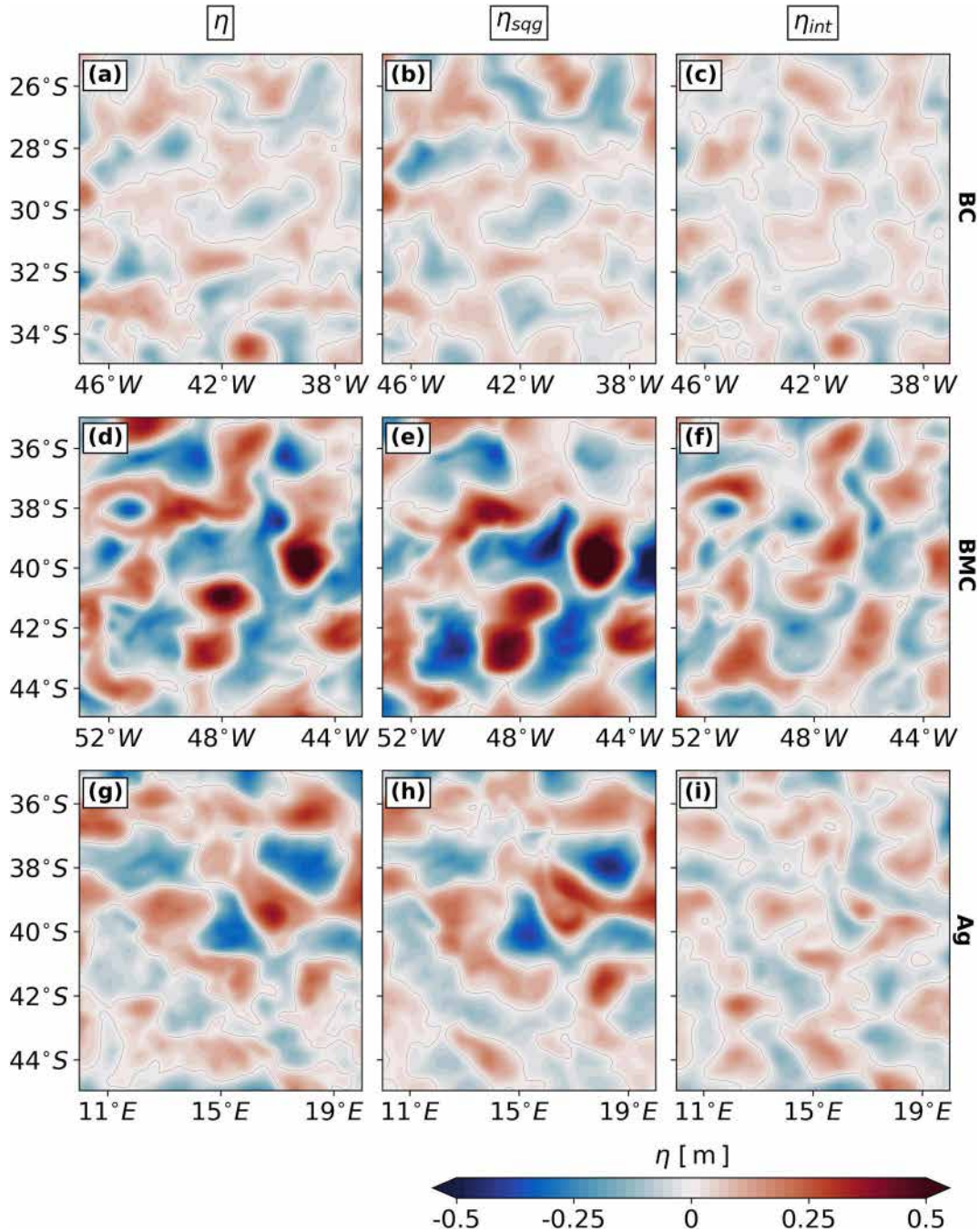

Figure 5. Sea surface height from HYCOM (η), SQG (η_{sqg}), and interior (η_{int}) reconstructions for the regions BC [19 July 2012, (a)–(c)], BMC [21 July 2008, (d)–(f)], and Ag [24 July 2011, (g)–(i)].

4.3. The Role of EKE and MLD

As previously discussed, the SQG reconstruction is largely dependent on a choice of areas and seasons. By and large, the reconstruction is better for regions with high mesoscale activity and a deeper mixed layer. To summarize our surface SQG reconstruction, we crossed the area-averaged EKE and MLD for the 5 years of model outputs, joining all three regions in a EKE-MLD grid displaying $(x_e, y_m) = (0.01\ m^2s^{-2}, 25\ m)$ cells. At each cell, we display the number of samples averaged and the median of the correlation (r) between ψ and ψ_{sqg} in Figure 6.

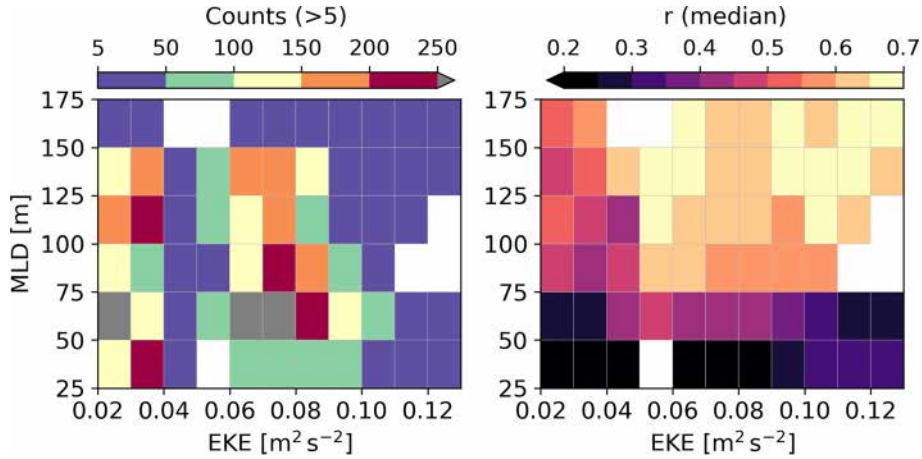

Figure 6. (a) Number of days (counts) for values of mean kinetic energy and mean mixed-layer depth in the EKE–MLD space, in regular grid cells of 0.01 $m^2 s^{-2}$, 25 m and (b) the median of the ψ and ψ_{sqg} correlations obtained at each EKE-MLD cell, for all three regions.

Since we selected peculiar regions with relative high, average, and low EKE throughout the year, Figure 6a presents a non-uniform distribution of counts (days) in the EKE-MLD space (we also masked regions with less than five counts). Daily averages with low and intermediate EKE spanned MLD values of 25–150 m, while deep MLD (>150 m) and high EKE (>0.10 $m^2 s^{-2}$) were less common. As previously discussed—and owing to the notion that EKE and MLD tend to be correlated—one would expect a linear increase of SQG correlations (r) with increasingly MLD and EKE. Although this progressive increase may be depicted from Figure 6b, a striking contrast in r—with a marked threshold for MLD $\simeq$ 75 m—highlights that the MLD plays a major role in the quality of the SQG reconstruction. As shown in Figures 4 and 6, correlations between ψ and ψ_{sqg} are higher for MLD deeper than 75 m. Surprisingly, during winter and early spring the dependence of EKE for the reconstruction was less evident even though the KE follows spectral slopes of $\sim k^{-5/3}$ (Figure 2). For a too-shallow MLD (<50 m), correlations between fields only start to increase for EKE exceeding 0.1 $m^2 s^{-2}$, even though they hardly reach $r = 0.35$. For MLD between <50 and 75 m, correlations are slightly higher, but no pattern can be associated with increasing EKE. However, when the mixed layer deepens, variations toward high EKE also yield larger correlations (Figure 6b), especially deeper than 75 m.

To summarize, we quantify the influence of the MLD over the EKE evaluating the changes in the MLD axis in respect to the EKE. Taking ΔM and ΔE as the relative increase in r due to the increase in MLD and EKE, respectively

$$\Delta \mathrm{M} = \frac{1}{x_e} \left. \frac{\Delta r_{(\mathrm{MLD})}}{\Delta \mathrm{MLD}} \right|_{25}^{175} \quad \text{and} \quad \Delta \mathrm{E} = \frac{1}{y_m} \left. \frac{\Delta r_{(\mathrm{EKE})}}{\Delta \mathrm{EKE}} \right|_{0.02}^{0.13}, \tag{11}$$

where multiplying by (x_e, y_m) in each direction guarantee ΔM and ΔE with same dimension $s^2\ m^{-3}$. Using these normalized quantities, the non-dimensional ratio,

$$\varepsilon = \frac{\Delta \mathrm{M}}{\Delta \mathrm{E}}, \tag{12}$$

compares the *mean* rate of change in r due to the MLD and EKE. The mean scenario in Equation 11 accounts for the full variation of r in the MLD and EKE directions. Applying Equation 11 to Equation 12 yields $\varepsilon \simeq 6$, meaning that the MLD is on average six times more important than the EKE in improving the SQG correlation r. Evaluating how discrete changes in MLD affect r, we used $\Delta \mathrm{M}|_{25}^{100}$ m and obtained $\varepsilon \simeq 9$, emphasizing the threshold set by the transition from relatively shallow (~25 m) to deep (>100 m) MLD. However, when the MLD is larger than 100 m ($\Delta \mathrm{M}|_{100}^{175}$ m), the contribution to the increase of r is equivalent for MLD and EKE, with $\varepsilon \simeq 1$. We therefore suggest that the MLD has a greater impact on the surface reconstruction, and that this reconstruction is bounded to the MLD dynamics.

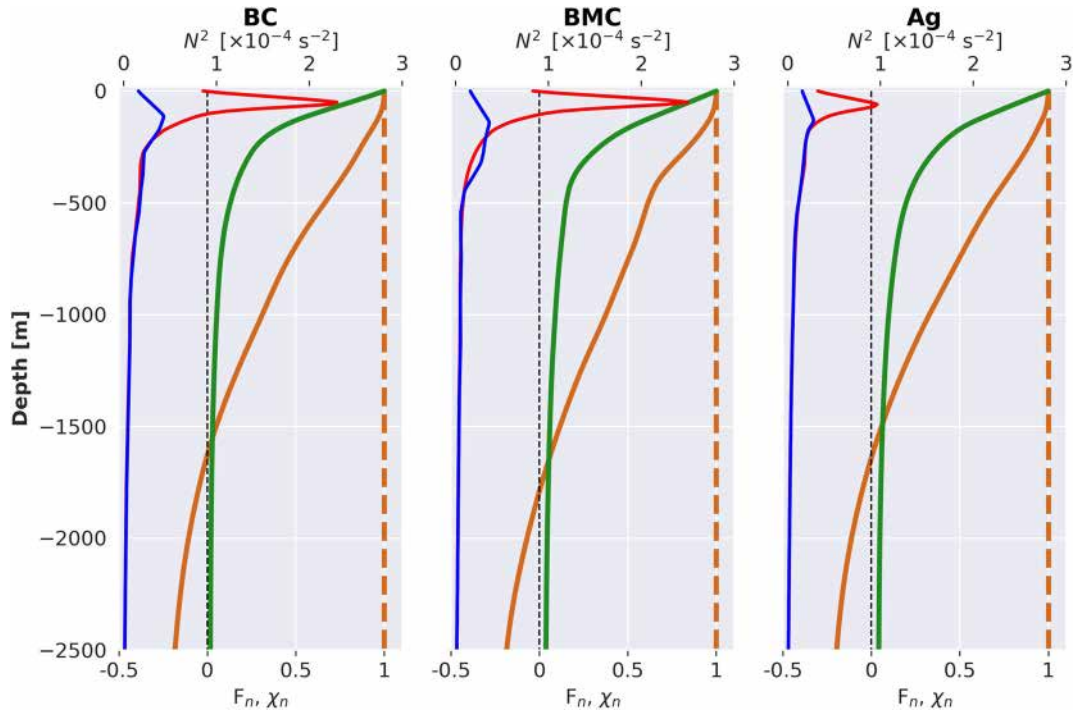

Figure 7. Brunt-Väisälä frequencies (N^2; upper horizontal axis) for a day in summer (red) and a day in winter (blue) and the normalized vertical modes (F_n, χ_n; bottom horizontal axis) for each area shown up to 2,500 m. The SQG solution (χ, green) and first baroclinic mode (F_1, solid brown) are depth dependent, whereas the barotropic mode (F_0, dashed brown) is depth-invariant.

So far, our surface reconstructions were capable of capturing most of the geostrophic motion, particularly during winter when the MLD is deeper. However, even with a deep mixed layer, the SQG surface alone does not suffice to characterize all the surface spatial patterns. This sets the stage for the isQG method (Wang et al., 2013), an improved reconstruction in which the total geostrophic stream function is derived from both SQG and QG solutions.

5. isQG: The Contribution of the Interior PV

To obtain the reconstruction of the vertical structure and its dynamical implications, we extended our surface results to the whole water column based on the linearity of the QG PV equation, so that the total stream function could be calculated as the sum of the contribution of surface (SQG) and interior (QG) dynamics, the latter including the barotropic and first-baroclinic modes (Ferrari & Wunsch, 2010; Lapeyre & Klein, 2006), as in Equation 3. Together, these solutions form the isQG method of reconstruction, outlined in Section 2 and described in detail by Wang et al. (2013).

As described earlier, to reconstruct the stream function associated with the SQG solution, only three parameters are required: a stratification profile, a buoyancy anomaly field and the sea surface height. At the surface, the difference between the pressure and the SQG solution is attributed to the interior solution as a truncation of the first two dynamical modes. The modal amplitudes are calculated assuming that these modes give the residual pressure at the surface and are forced to be zero at the bottom, like the SQG solution. Combining the vertical structures of the SQG (Equation 6) and QG (Equation 7) contributions, we account for most of the residual pressure not captured by SQG at the surface, and correlations between HYCOM's and the reconstructed stream functions reach values greater than 0.98 for the three regions and periods analyzed. However, a good reconstruction at the surface does not necessarily indicate a good reconstruction at depth.

We show the stratification profiles for a day in winter and summer and the normalized vertical structure of SQG (χ) and QG ($F_{0,1}$) solutions for each area in Figure 7. The SQG solution (Figure 7, green line) is an exponential-decaying profile, intensified near the surface. As a result of the 2-mode truncation (see Equation 7), the QG

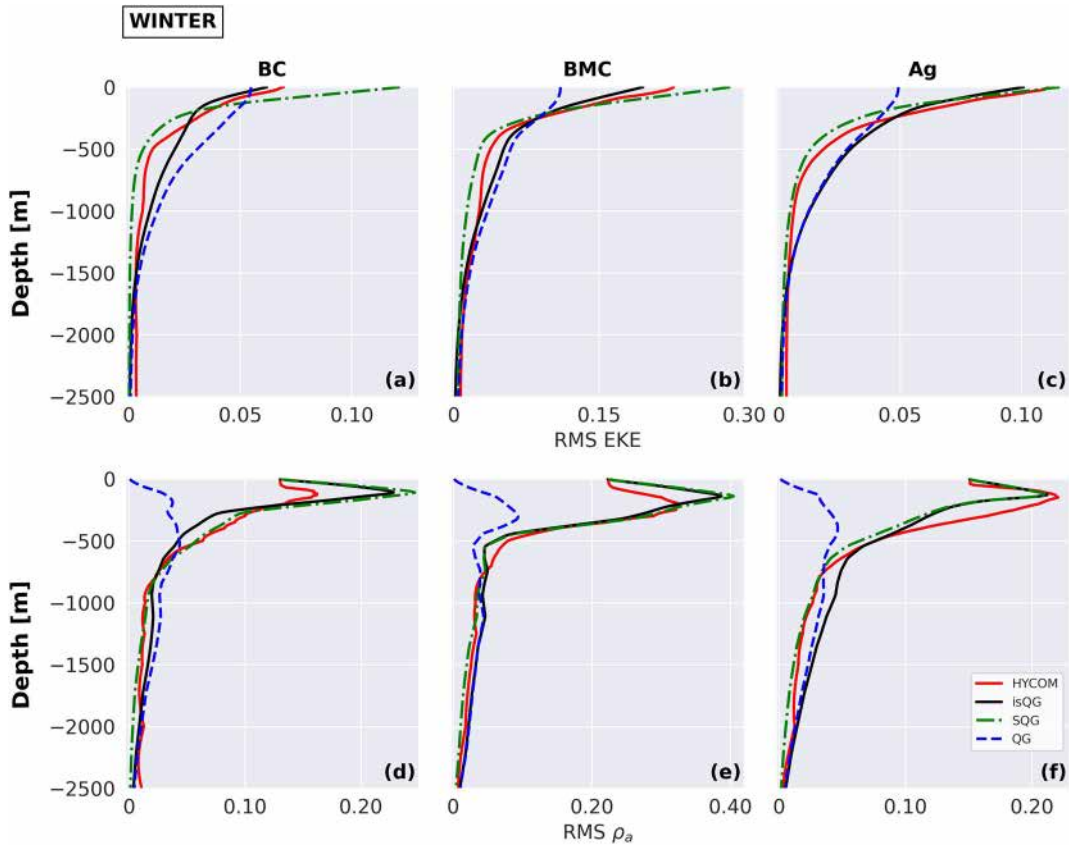

Figure 8. Root mean square (RMS) of eddy kinetic energy and density anomalies (ρ_a) for the BC (a) and (d), BMC (b) and (e), and Ag (c) and (f) regions derived from ψ_{sqg} (green), ψ_{int} (blue), ψ_{isQG} (black), and ψ from HYCOM (red) for a day in winter.

solutions include the depth-invariant barotropic mode (Figure 7, dashed brown line) and the first baroclinic mode (Figure 7, solid brown line), also surface intensified. Differences between the N^2 profiles for a day in winter and summer (Figure 7, blue and red lines) are readily depicted. In all areas, stratification in summer is at least 10 times stronger than stratification in winter.

We evaluated the quality of our isQG reconstruction in terms of the root-mean-square (RMS) of the density anomalies (ρ_a), given by

$$\rho_a = -\frac{\rho_0 f_0}{g}\frac{\partial \psi}{\partial z}, \tag{13}$$

and the RMS EKE, obtained from the model velocities $\mathbf{v} = (u, v)$. The horizontal and vertical structure of the RMS perturbation KE for each solution is given by $\mathrm{EKE}_{sqg} = \mathbf{v}^2_{sqg}/2$ and $\mathrm{EKE}_{int} = \mathbf{v}^2_{int}/2$, with $\mathbf{v}(x, y, z, t)$. Since the SQG solutions and interior QG modes are not orthogonal, the total EKE (EKE_{isQG}) must also include the cross-correlation terms of the contributions,

$$EKE_{isQG} = EKE_{sqg} + EKE_{int} + \mathbf{v}_{sqg}\mathbf{v}_{int}. \tag{14}$$

Below, we compare the RMS EKE and RMS ρ_a for each solution, SQG, QG, and isQG with the original model fields from HYCOM.

The vertical structure of the model velocities in terms of RMS EKE is fairly represented by the isQG reconstructions in all regions for a day in winter (Figure 8), with discrepancies mostly confined to the pycnocline. This agreement is particularly noticeable in the upper ocean, above 400 m, where the SQG solution dominates and drive the isQG reconstruction, whereas the interior solution prevails below 500 m. Such regime shift is clear in

the Ag region (Figure 8c), which depicts both isQG and SQG curves aligned with the model velocities in the upper ocean. At the base of mixed layer, QG dynamics take over the solution, dominating the isQG reconstruction thereon. This pattern is repeated for the BMC (Figure 8b), but is less clear for the BC region (Figure 8a). At these two regions, Figures 8a and 8b show that the SQG solution overestimates model velocities close to the surface, suggesting that the interior solution has an important contribution in the isQG solution. In Ag, the RMS EKE of the SQG solution compares to HYCOM for the whole water column. At the surface, the strong similarity between HYCOM and SQG vertical patterns in Figure 8c agrees with results from Section 4, where we found the higher correlations between ψ and ψ_{sqg} for this region. The strong dominance of SQG in winter suggests that, during this season, the SSH is closely related to surface dynamics. When smaller-scales develop in winter, the spectral slope is flattened toward $k^{-5/3}$ (Figure 2), and SSH thus reflects the surface solution.

The RMS density anomalies (Figures 8d–8f) shows consistency between the density from HYCOM, the SQG, and the isQG solutions, although these reconstructions overestimate the model density in BC and BMC within the mixed layer and underestimate it in Ag at the pycnocline. The solutions capture the vertical structure of density in the upper ocean due to buoyancy anomalies not null at the surface when inverting the PV equation. As for the interior solution, density anomalies are zero at the surface, by definition. This contributes to the fact that the interior QG solutions fail to capture the vertical structure and amplitude of the density anomalies in all areas. At deeper layers, all three solutions adequately represent the model, although the SQG solution seems to produce better results, particularly for Ag.

According to Lapeyre and Klein (2006), both buoyancy anomalies and mesoscale PV can be forced by baroclinic instabilities at large scales. The authors showed that the interior PV in the upper ocean is correlated with the surface buoyancy, thus for the first 500 m a "surface trapped" solution would be a good representation of the total stream function. Although not a golden rule, this is well represented by our Ag region (Figure 8c) in winter, since the SQG ρ_a and EKE fit the model's velocity and density structure. This is also in agreement with the performance of the SQG reconstruction discussed in Section 4, where Ag presented the largest correlations of all regions, even in summer, as shown below.

During summer, the mixed layer is shallower, which causes the decoupling of the sea surface density from the interior dynamics, as discussed by Wang et al. (2013). Since our SQG performance depends on such coupling, the solutions under this condition become compromised (Figures 9a–9c). The interior solution dominates isQG, which best correlates HYCOM. Yet, the SQG contribution to isQG enhances the surface representation of the model velocities, being slightly larger in Ag than in BC and BMC. Moreover, the strong influence of the interior would implicate that SSH mainly reflects the interior dynamics. For the RMS density, Figures 9d–9f show that selecting only the first two dynamical modes in the interior solution yields a poor representation of the density field in the upper layer (e.g., Wang et al., 2013). In the isQG solution, the SQG contribution enhances the representation of the pycnocline, although it usually overestimates the model density within the mixed layer. Below 500 m, the SQG contribution is nearly null, and isQG closely follows the interior solution, presenting the best representation of the model density. For our regions, stratification is stronger in summer (Figure 7), and this strong stratification is capable of suppressing the contribution of the SQG solution to isQG (Liu et al., 2014). Moreover, the density anomalies from the isQG decay much faster than the ones from the model from around 200 m (Figures 9d–9f).

In the isQG theory, the total stream function is derived from SSH, and isQG velocities are geostrophic. Therefore, the discrepancy noted in the top panels of both Figures 8 and 9, in which surface EKE from isQG differ from HYCOM's, are likely due to the existence of ageostrophic flows in the model. However, the flow is largely geostrophic, and the ageostrophic component would not affect significantly the reconstruction. For the Ag region, a comparison between horizontal fields in Figure 10 shows that the isQG method is able to capture the horizontal structures and the overall magnitude of the density anomaly field at different depths. The reconstruction is best for the upper layers and at 500 m (Figures 8f and 10b–10f), but decays from about 80 m, where the isQG reconstructed fields are weaker than HYCOM's. At 80 m, isQG can capture most of the horizontal mesoscale patterns in detail, for example, the mesoscale feature north of 38°S and east of 14°E (Figures 10a and 10b). The deeper we go, the fainter the isQG reconstruction becomes (Figure 10g), but the overall shape and magnitude of structures are represented (Figurea 10c–10f). Correlations at depth (Figure 10g) are higher than 0.92 (0.6) for the first 100 (1,250) m, but the reconstruction still degrade at higher depths. In addition, our isQG reconstruction is

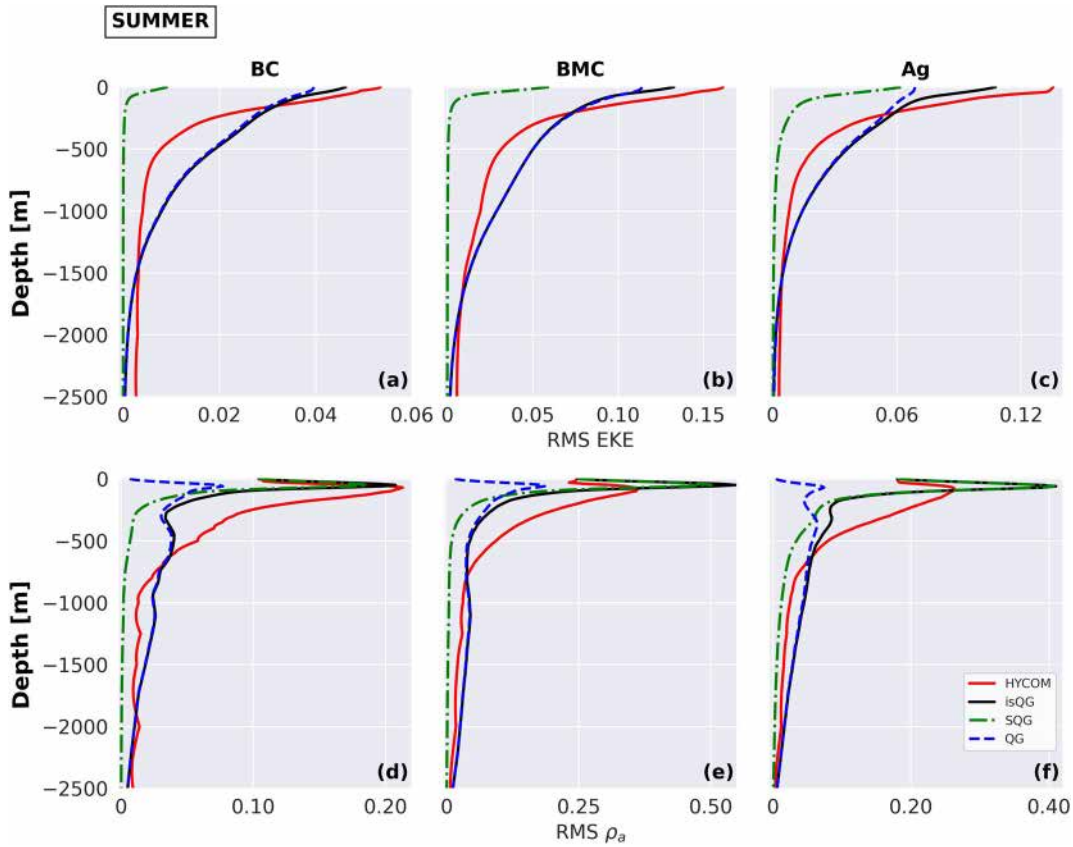

Figure 9. Root mean square (RMS) of eddy kinetic energy (EKE) and density anomalies (ρ_a) for the BC (a),(d), BMC (b),(e), and Ag (c),(f) regions derived from ψ_{sqg} (green), ψ_{int} (blue), ψ_{isQG} (black), and ψ from HYCOM (red) for a day in summer.

also scale-dependent and performs better with wavelengths larger than 100 km. Below 100 m depth, the spectral correlations (not shown) drop from 0.97 to 0.70 toward the short mesoscale, that is, <100 km.

For the velocity structure, we have compared relative vorticity fields. (The velocity derivatives tend to amplify noise, providing a stricter test for our reconstruction.) Figure 11 shows that isQG and HYCOM patterns are consistent for the upper layer (Figures 11a and 11b), but the reconstruction degrades with depth much faster than the density fields (Figure 11g). Correlations between vorticity fields at above 80 m are larger than 0.88, but at 500 m (1,000 m) it drops drastically to 0.49 (0.3). Contrary to density, the reconstructed fields are weaker than the model's at 80 m (Figures 11a and 11b), and the inverse occur below for 500 and 1,000 m (Figures 8c and 11e–11f). Similarly to the density field, our vorticity reconstruction also depend on scale. In this case, the spectral correlation already decreases on the surface toward the short mesoscale, dropping from 0.97 at 400 km to 0.76 at 30 km. All areas presented the aforementioned drop in spectral correlation at wavelengths around 100 km in winter. During summer, this scale dependency is not clear for the density fields at BC and BMC, and spectral correlations are approximately constant (~0.7) through wavelengths. As for the Ag region, the spectral correlations between the model and the reconstructed ρ_a drops at around 150 km.

6. Discussion

Using outputs from a numerical model reanalysis, we showed that the SQG and isQG methods can reproduce surface and interior dynamics, to a greater or lesser extent, under different conditions. However, the main motivation to develop both methods resides in the ability to infer ocean dynamics below the surface, using, for example, satellite data. The ability to correctly observe and represent ocean dynamics has always been a challenge for the scientific community, and huge progress was made since the first altimeters were able to accurately measure ocean topography (e.g., Stammer, 1997; Wunsch, 1997; Wunsch & Stammer, 1995). Up to today, altimeters resolve

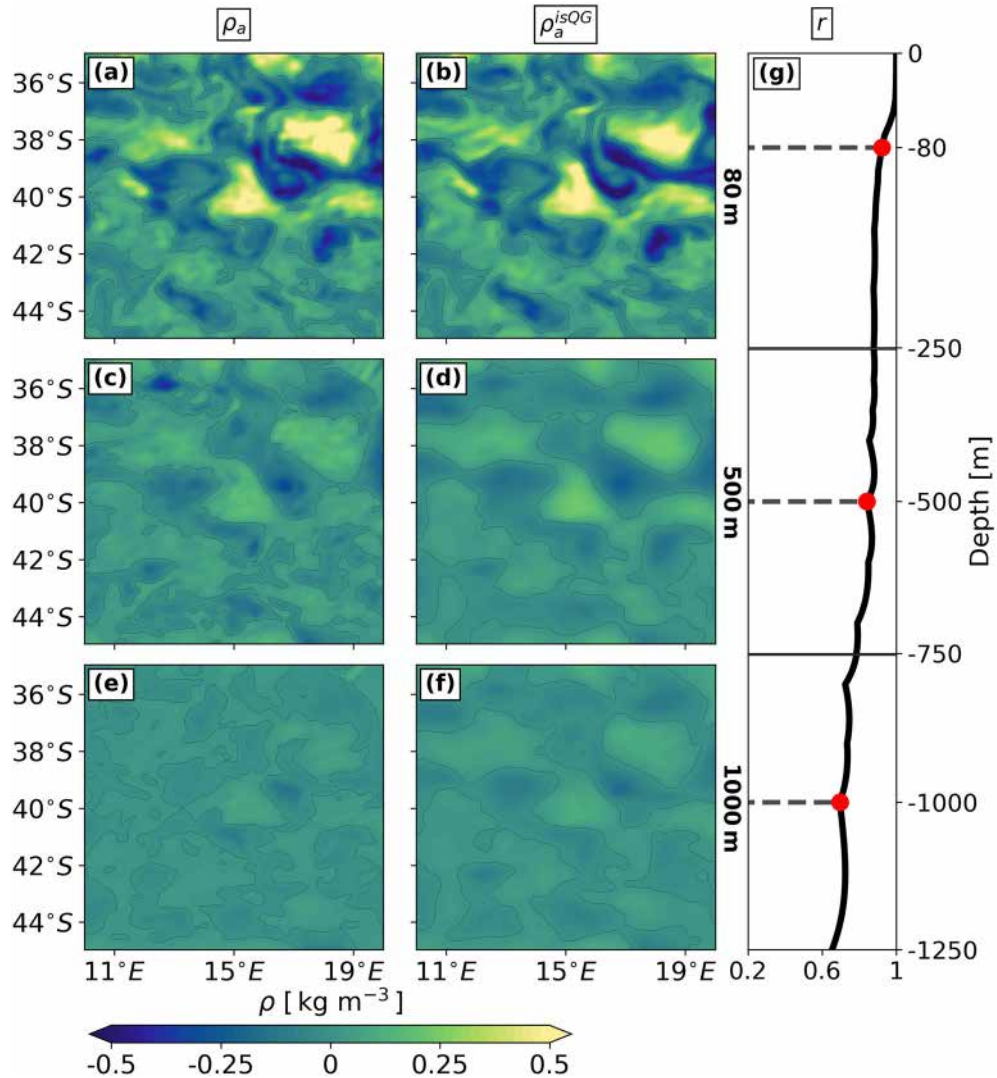

Figure 10. Density anomalies from HYCOM (a), (c), and (e) and the isQG method (b), (d), and (f) and their spatial correlations (g) at 80, 500, and 1,000 m (red dots) for the Ag region on 24 July 2011.

horizontal scales around 100–150 km (Xu & Fu, 2012), with smaller scales associated with mesoscale motions remaining a challenge. Thus, applying the SQG and isQG methods on observations guarantees the dynamics at scales coarser than 100 km. In addition to the resolution, there are other issues associated with the reconstruction of ocean currents from satellite observations, such as density measurements. Reconstruction attempts were also made using SSS from SMOS (Isern-Fontanet et al., 2016; Liu et al., 2017) to obtain surface density. But with an average spatial resolution of 43 km, a significant part of the ocean variability associated with the smaller scales is still missing. Salinity observations from remote sensing strongly rely on in situ data for calibration and quality control, and although great improvement was attained since the implementation of SSS observation networks, such as the Voluntary Observing Ships from the French SSS Observation Service (Alory et al., 2015), global coverage is far from being achieved. Therefore the community urges for better salinity observations, especially in high latitudes (Martínez et al., 2021; Vinogradova et al., 2019).

Another constraint to obtain subsurface circulation from the SQG (and isQG) method using satellite data is the lack of availability of daily stratification profiles. In situ data is scarce and regionally concentrated. The flow reconstruction would still be possible with a monthly averaged climatological N^2 profile. However, decreasing the resolution from daily to monthly scales would reduce drastically the short mesoscale signal of the fields (SSH, buoyancy), and thus the effectiveness of the SQG method. The stream function does not follow the SQG solution

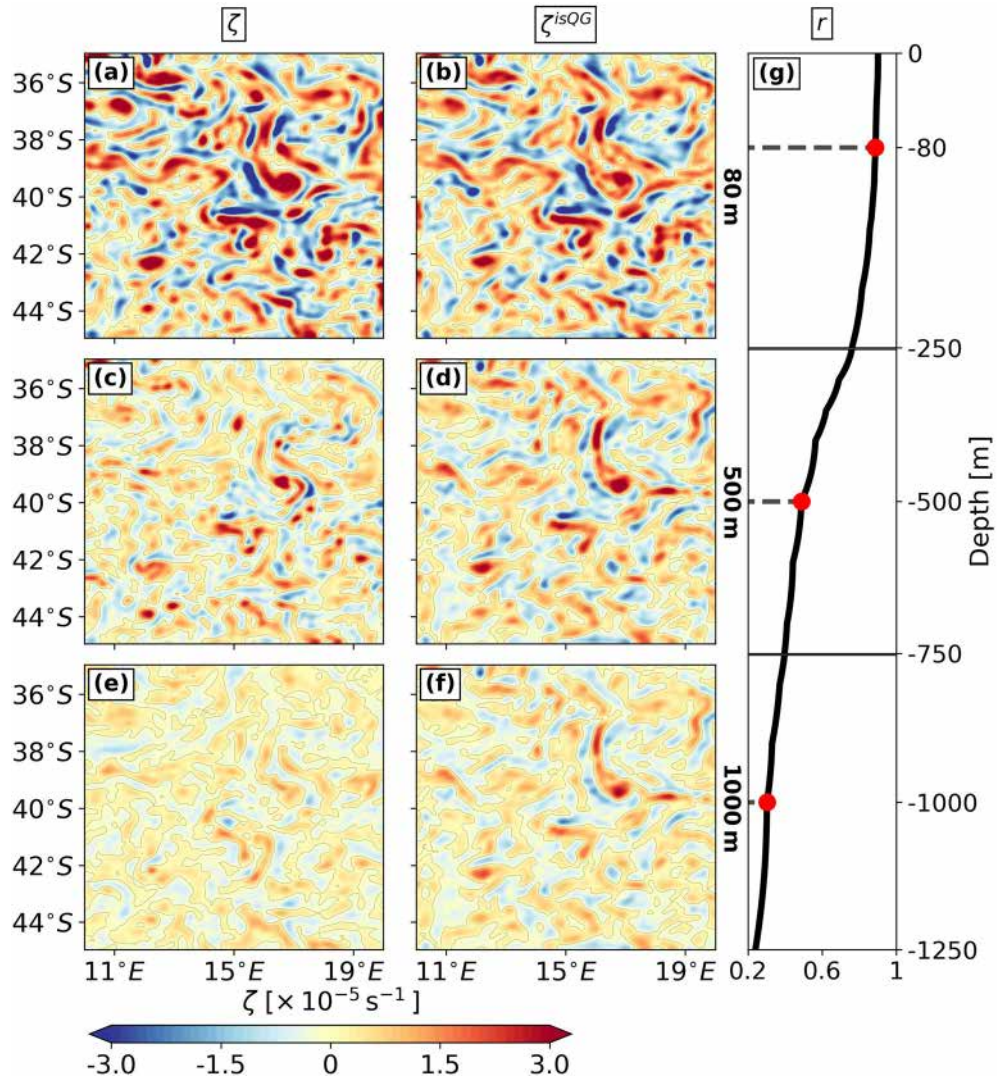

Figure 11. Relative vorticity from HYCOM (a), (c), (e) and the isQG method (b), (d), and (f) and their spatial correlations (g) at 80, 500, and 1,000 m (red dots) for the Ag region for 24 July 2011.

for large scales (e.g., Isern-Fontanet et al., 2014), yielding therefore lower correlations for averaged fields. A better scenario arise from the eSQG method (Lapeyre & Klein, 2006), which uses constant stratification to derive analytical solutions. The main advantages of such method are that the surface stratification could be obtained from temperature and salinity either from satellites, in situ data, and numerical models, and it is computationally inexpensive if compared to the isQG method. Previous studies (see Isern-Fontanet et al., 2008; Lapeyre & Klein, 2006; Qiu et al., 2020) showed that the eSQG is an efficient method for the reconstruction, however, it generally only works in the upper layers (<500 m) and the representation of density fields are not as satisfactory as the one obtained with the isQG method (Liu et al., 2019).

Our isQG reconstruction is generally consistent with HYCOM's energy and density-anomaly structure, particularly above 500 m and for wavelengths larger than 100 km. Within the pycnocline, the isQG reconstruction overestimates EKE and underestimates density (Figures 8 and 9). A possible explanation for these differences point to the regionally averaged N^2 because all the spatial variability is eliminated once we average the stratification into one single profile. Another possible explanation is the lack of higher modes, where the barotropic and the first-baroclinic modes are not sufficient to describe the flow structure, especially below the pycnocline where such modes have a higher relative contribution. Liu et al. (2019) addressed this limitation at a subdomain of the Kuroshio Current using a submesoscale resolving model with high resolution (1/30°). Partitioning the residual

(model−SQG) KE into QG modes, the authors showed that the barotropic mode dominates the spectrum up to 150 km but loses importance toward smaller scales, when higher (≥2) modes become significant. Thus, the isQG fails to project the smaller-scales from the residual fields [i.e., $\psi_{int}(z = 0)$] that reflect these higher-order modes downward (Liu et al., 2019), consequently resulting in deceptive features (Figures 11e and 11f). To surpass this caveat, the authors propose a scale-dependent vertical projection of SSH and bring together both isQG and eSQG methods: for wavelengths smaller (larger) than 150 km, the flow reconstruction invokes the eSQG (isQG) method, with the upper boundary condition for the eSQG being the SSH.

Even though our model's resolution is not as high as the one used by Liu et al. (2019), we were able to identify the isQG limitation in the deep layers in both density and vorticity reconstruction, especially below 500 m (Figures 10 and 11). This is particularly apparent in the vorticity reconstructions because the horizontal derivatives enhance the smaller-scale features. Spatial correlations drop from 0.89 to 0.5 and 0.30 at 80, 500, and 1,000 m (Figure 11g). At 500 m, our correlation between the model and the reconstructed vorticity is 19% larger than the correlation reported by Liu et al. (2019), suggesting that the model's resolution can also play an important role on the reconstruction's depiction of the smaller-scale features. As for the density reconstruction, the isQG limitation is barely noticed because the smaller-scales that are (falsely) projected to greater depths are eliminated by the stream function's vertical derivative (Figures 10e and 10f). Nevertheless, the isQG reconstruction drastically reduces the strong seasonal differences previously observed with the SQG reconstruction. With a threshold of 0.75 (0.5) correlation, the isQG can reproduce the model's vorticity above 270 (500) m. For density fields, the same thresholds yield a good reconstruction above 880 (1,730) m.

Expectation surrounds the upcoming Surface Water and Ocean Topography (SWOT) mission, where sea surface height will be measured in 2D along a wide swath, considerably improving horizontal resolution and allowing a better estimation of spatial gradients. The mission's main objective is to characterize mesoscale and upper portions of the submesoscale variability from surface topography, promising resolved scales of 15–30 km, depending on the sea state (Morrow et al., 2019). Processes at these scales are highly energetic and dissipative, affecting the ocean global and regional energy budgets. They also create strong gradients (e.g., temperature and salinity) that connect surface and interior dynamics. With SWOT's wide-swath radar being capable of characterize these processes (e.g., Qiu et al., 2016, 2020), we would increase our understanding of the inverse energy cascade, baroclinic internal tides, and internal gravity waves, processes that share a great portion of the variability of the sea surface height (e.g., Richman et al., 2012; Rocha, Chereskin, et al., 2016; Qiu et al., 2020), which would also reflect on better configuration of general ocean circulation models. In HYCOM, for instance, there is a clear seasonal cycle in both the KE spectral slopes and our SQG reconstruction, which may be associated with instabilities of a deep mixed layer (Callies & Ferrari, 2013; Sasaki et al., 2014).

Lastly, SWOT will also bring a different perspective in terms of SSH wavenumber spectra and spectral slopes. Both SQG and QG theories predict different exponents for the spectra of KE and SSH, which is an indicative of the region's dynamics. Although spectral slopes over the mesoscale range from along-track altimetry are consistent with the turbulence theories (Vergara et al., 2019; Wang et al., 2019) in highly energetic regions, the reasons for the flatter spectra found in low-energy regions still poses an ongoing debate (Richman et al., 2012; Rocha, Chereskin, et al., 2016; Sasaki et al., 2014; Uchida et al., 2017). In this context, improved theoretical framework should be pursued. Possible suggestions are considering a 3D instead of a regionally averaged stratification when solving Equation 4, distinguishing between a surface and subsurface intensified flows (Assassi et al., 2016), and employing methods that benefit from additional considerations (e.g., Liu et al., 2019; Yan et al., 2020). We expect to overcome these challenges in a near future, with the possibility to extend our findings based on ocean general circulation models to high-resolution altimeter observations.

7. Summary and Conclusions

The BC, BMC, and Ag regions are the most energetic regions on the South Atlantic. In these regions, a seasonal cycle in the spectral slopes suggests a change in the dynamics from a SQG to QG regime. During austral winter, slopes of the three areas are close to the SQG predictions, with peaks in late winter and early spring. In summer, the slopes better followed the QG regime (Figure 2).

The SQG reconstruction for the selected areas shows strong dependence to the seasonality of the mixed layer (Figures 3 and 4), especially when reconstructed using density anomalies. With a deep mixed layer in winter, the

SQG capture most mesoscale structures and their magnitude, with the correlations between the SSH from the model and the reconstructed SQG SSH reaching on average 0.61 in all regions, with maximum of 0.83 in the Ag (Figure 5). Compared with the EKE, the MLD drives the quality of the SQG reconstruction, especially in areas with shallower MLD, where changes in MLD are nine times more important than changes in EKE to improve correlations (Figure 6). For MLDs deeper than 75 m, the contribution of MLD and EKE is nearly equal.

The inclusion of the interior (QG) solution as part of the isQG method not only raised the correlations in all fields (SSH, velocity, and vorticity), implying that the spatial patterns are better resolved, but also corrected the discrepancies in magnitude seen in some locations within our areas, raising surface correlations to at least 0.98. To reconstruct the vertical structure (Figures 8 and 9), the SQG solution alone is capable of characterize HYCOM's stream function during winter, whereas the interior solution dominates during summer. However, by combining both solutions into the isQG method, the reconstruction is improved considerably, yet some underestimation of the surface energy and the pycnocline is still present in summer, probably due to the truncation of only the first two QG modes. One caveat is that the isQG reconstruction degrades with depth (Liu et al., 2019), and small-scale features are falsely projected through the water column, yielding a good reconstruction above 270 (500) m with a 0.75 (0.5) correlation threshold for our vorticity fields (Figure 11). This limitation is not so clear for the density reconstruction (Figure 10). Nevertheless, the isQG reconstructed velocity and density anomalies are consistent with the model in all regions, showing the potential of applying the methodology on the South Atlantic (Figures 10 and 11).

Data Availability Statement

HYCOM reanalysis outputs (GLBu0.08/expt_19.1) analyzed in this study can be found at hycom.org/data/glbu0pt08/expt-19pt1.

Acknowledgments
We would like to acknowledge the financial support of Conselho Nacional de Desenvolvimento Científico e Tecnológico—CNPq (130215/2018-0) and Fundação de Amparo à Pesquisa do Estado de São Paulo—FAPESP (2019/02968-9, 2019/13830-8, and 2017/09659-6). This work was supported in part by the Spanish R&D project L-BAND (ESP2017-89463-C3-1-R), which is funded by MCIN/AEI/10.13039/501100011033 and "ERDF A way of making Europe," and project INTERACT (PID2020-114623RB-C31), which is funded by MCIN/AEI/10.13039/501100011033. We also acknowledge the financial support from the Spanish government through the "Severo Ochoa Centre of Excellence" accreditation (CEX2019-000928-S). This work is a contribution to CSIC PTI Teledetect. This work supports the SWOT-Brésil project, in preparation for the future SWOT wide-swath altimetry mission. SWOT-Brésil project is financed by CNES/INSU via the French TOSCA programme.

References

Aguedjou, H. M. A., Dadou, I., Chaigneau, A., Morel1, Y., & Alory, G. (2019). Eddies in the tropical Atlantic Ocean and their seasonal variability. *Geophysical Research Letters*, *46*, 12156–12164. https://doi.org/10.1029/2019gl083925

Alory, G., Delcroix, T., Téchiné, P., Diverrès, D., Varillon, D., Cravatte, S., et al. (2015). The French contribution to the voluntary observing ships network of sea surface salinity. *Deep Sea Research Part I: Oceanographic Research Papers*, *105*, 1–18. https://doi.org/10.1016/j.dsr.2015.08.005

Assassi, C., Morel, Y., Vandermeirsch, F., Chaigneau, A., Pegliasco, C., Morrow, R., et al. (2016). An index to distinguish surface-and subsurface-intensified vortices from surface observations. *Journal of Physical Oceanography*, *46*(8), 2529–2552. https://doi.org/10.1175/jpo-d-15-0122.1

Blumen, W. (1978). Uniform potential vorticity flow: Part I. Theory of wave interactions and two-dimensional turbulence. *Journal of the Atmospheric Sciences*, *35*, 774–783. https://doi.org/10.1175/1520-0469(1978)035<0774:upvfpi>2.0.co;2

Brum, A. L., de Azevedo, J. L. L., de Oliveira, L. R., & Calil, P. H. R. (2017). Energetics of the Brazil Current in the Rio Grande Cone region. *Deep Sea Research Part I: Oceanographic Research Papers*, *128*, 67–81. https://doi.org/10.1016/j.dsr.2017.08.014

Callies, J., & Ferrari, R. (2013). Interpreting energy and tracer spectra of upper-ocean turbulence in the submesoscale range (1–200 km). *Journal of Physical Oceanography*, *43*, 2456–2474. https://doi.org/10.1175/jpo-d-13-063.1

Callies, J., Ferrari, R., Klymak, J. M., & Gula, J. (2015). Seasonality in submesoscale turbulence. *Nature Communications*, *6*(1), 1–8. https://doi.org/10.1038/ncomms7862

Chassignet, E. P., Hurlburt, H. E., Metzger, E. J., Smedstad, O. M., Cummings, J. A., Halliwell, G. R., et al. (2009). US GODAE: Global ocean prediction with the HYbrid Coordinate Ocean model (HYCOM). *Oceanography*, *22*(2), 64–75. https://doi.org/10.5670/oceanog.2009.39

Cummings, J. A. (2005). Operational multivariate ocean data assimilation. *Quarterly Journal of the Royal Meteorological Society*, *131*(613), 3583–3604. https://doi.org/10.1256/qj.05.105

de Boyer Montégut, C., Madec, G., Fischer, A. S., Lazar, A., & Iudicone, D. (2004). Mixed layer depth over the global ocean: An examination of profile data and a profile-based climatology. *Journal of Geophysical Research: Oceans*, *109*(C12). https://doi.org/10.1029/2004jc002378

Dufau, C., Orsztynowicz, M., Dibarboure, G., Morrow, R., & Traon, P.-Y. L. (2016). Mesoscale resolution capability of altimetry: Present and future. *Journal of Geophysical Research: Oceans*, *121*, 4910–4927. https://doi.org/10.1002/2015jc010904

Ferrari, R., & Wunsch, C. (2009). Ocean circulation kinetic energy: Reservoirs, sources, and sinks. *Annual Review of Fluid Mechanics*, *41*, 253–282. https://doi.org/10.1146/annurev.fluid.40.111406.102139

Ferrari, R., & Wunsch, C. (2010). The distribution of eddy kinetic and potential energies in the global ocean. *Tellus A: Dynamic Meteorology and Oceanography*, *62*(2), 92–108. http://doi.org/10.1111/j.1600-0870.2009.00432.x

Fu, L.-L., Chelton, D. B., Le Traon, P.-Y., & Morrow, R. (2010). Eddy dynamics from satellite altimetry. *Oceanography*, *23*(4), 14–25. https://doi.org/10.5670/oceanog.2010.02

Garzoli, S. L., & Garraffo, Z. (1989). Transports, frontal motions and eddies at the Brazil-Malvinas currents confluence. *Deep Sea Research Part I: Oceanographic Research Papers*, *36*(5), 681–703. https://doi.org/10.1016/0198-0149(89)90145-3

González-Haro, C., & Isern-Fontanet, J. (2014). Global ocean current reconstruction from altimetric and microwave SST measurements. *Journal of Geophysical Research: Oceans*, *119*, 3378–3391. https://doi.org/10.1002/2013JC009728

González-Haro, C., Isern-Fontanet, J., Tandeo, P., & Garello, R. (2020). Ocean surface currents reconstruction: Spectral characterization of the transfer function between SST and SSH. *Journal of Geophysical Research: Oceans*, *125*(10), 1–16. https://doi.org/10.1029/2019JC015958

Gordon, A. L., & Haxby, W. F. (1990). Agulhas eddies invade the South Atlantic: Evidence from Geosat altimeter and shipboard conductivity-temperature-depth survey. *Journal of Geophysical Research: Oceans*, *95*(C3), 3117–3125. https://doi.org/10.1029/jc095ic03p03117

Held, I. M., Pierrehumbert, R. T., Garner, S. T., & Swanson, K. L. (1995). Surface quasi-geostrophic dynamics. *Journal of Fluid Mechanics*, *282*, 1–20. https://doi.org/10.1017/s0022112095000012

Hoskins, B. J., McIntyre, M. E., & Robertson, A. W. (1985). On the use and significance of isentropic potential vorticity maps. *Quarterly Journal of the Royal Meteorological Society*, *111*(470), 877–946. https://doi.org/10.1002/qj.49711147002

Houry, S., Dombrowsky, E., Mey, P. D., & Minster, J.-F. (1987). Brunt-Väisälä frequency and Rossby radii in the south Atlantic. *Journal of Physical Oceanography*, *17*, 1619–1626. https://doi.org/10.1175/1520-0485(1987)017<1619:bvfarr>2.0.co;2

Isern-Fontanet, J., Ballabrera-Poy, J., Turiel, A., & García-Ladona, E. (2017). Remote sensing of ocean surface currents: A review of what is being observed and what is being assimilated. *Nonlinear Processes in Geophysics*, *24*, 613–643. https://doi.org/10.5194/npg-24-613-2017

Isern-Fontanet, J., Chapron, B., Lapeyre, G., & Klein, P. (2006). Potential use of microwave sea surface temperatures for the estimation of ocean currents. *Geophysical Research Letters*, *33*(L24608), 1–5. https://doi.org/10.1029/2006gl027801

Isern-Fontanet, J., García-Ladona, E., González-Haro, C., Turiel, A., Rosell-Fiechi, M., Company, J., & Padial, A. (2021). High resolution ocean currents from sea surface temperature observations: The Catalan Sea (Western Mediterranean). *Remote Sensing*, *13*(18), 3635. https://doi.org/10.3390/rs13183635

Isern-Fontanet, J., García-Ladona, E., Jiménez-Madrid, J. A., Olmedo, E., García-Sotillo, M., Orfila, A., & Turiel, A. (2020). Real-time reconstruction of surface velocities from satellite observations in the Alboran Sea. *Remote Sensing*, *12*(4), 724. https://doi.org/10.3390/rs12040724

Isern-Fontanet, J., & Hascoët, E. (2014). Diagnosis of high resolution upper ocean dynamics from noisy sea surface temperature. *Journal of Geophysical Research*, *118*, 1–132. https://doi.org/10.1002/2013JC009176

Isern-Fontanet, J., Lapeyre, G., Klein, P., Chapron, B., & Hecht, M. W. (2008). Three-dimensional reconstruction of oceanic mesoscale currents from surface information. *Journal of Geophysical Research*, *113*(C09005), 1–17. https://doi.org/10.1029/2007jc004692

Isern-Fontanet, J., Olmedo, E., Turiel, A., Ballabrera-Poy, J., & García-Ladona, E. (2016). Retrieval of eddy dynamics from SMOS sea surface salinity measurements in the Algerian Basin (Mediterranean Sea). *Geophysical Research Letters*, *43*(12), 6427–6434. https://doi.org/10.1002/2016gl069595

Isern-Fontanet, J., Shinde, M., & González-Haro, C. (2014). On the transfer function between surface fields and the geostrophic stream function in the Mediterranean Sea. *Journal of Physical Oceanography*, *44*, 1406–1423. https://doi.org/10.1175/jpo-d-13-0186.1

Klein, P., Isern-Fontanet, J., Lapeyre, G., Roullet, G., Danioux, E., Chapron, B., & Sasaki, H. (2009). Diagnosis of vertical velocities in the upper ocean from high resolution sea surface height. *Geophysical Research Letters*, *36*(12). https://doi.org/10.1029/2009gl038359

LaCasce, J. H. (2012). Surface quasigeostrophic solutions and baroclinic modes with exponential stratification. *Journal of Physical Oceanography*, *42*, 569–580. https://doi.org/10.1175/jpo-d-11-0111.1

LaCasce, J. H., & Mahadevan, A. (2006). Estimating subsurface horizontal and vertical velocities from sea-surface temperature. *Journal of Marine Research*, *64*, 695–721. https://doi.org/10.1357/002224006779367267

Lapeyre, G. (2009). What vertical mode does the altimeter reflect? On the decomposition in baroclinic modes and on a surface-trapped mode. *Journal of Physical Oceanography*, *39*, 2857–2874. https://doi.org/10.1175/2009jpo3968.1

Lapeyre, G., & Klein, P. (2006). Dynamics of the upper oceanic layers in terms of surface quasigeostrophy theory. *Journal of Physical Oceanography*, *36*, 165–176. https://doi.org/10.1175/jpo2840.1

Legeckis, R., & Gordon, A. L. (1982). Satellite observations of the Brazil and Falkland currents–1975 1976 and 1978. *Deep Sea Research Part I: Oceanographic Research Papers*, *29*(3), 375–401. https://doi.org/10.1016/0198-0149(82)90101-7

Le Traon, P. Y., Klein, P., Hua, B. L., & Dibarboure, G. (2008). Do altimeter wavenumber spectra agree with the interior or surface quasigeostrophic theory? *Journal of Physical Oceanography*, *38*, 1137–1142. https://doi.org/10.1175/2007jpo3806.1

Lima, M. O., Cirano, M., Mata, M. M., Goes, M., Goni, G., & Baringer, M. (2016). An assessment of the Brazil current baroclinic structure and variability near 22°S in distinct ocean forecasting and analysis systems. *Ocean Dynamics*, *66*(6–7), 893–916. https://doi.org/10.1007/s10236-016-0959-6

Liu, L., Peng, S., & Huang, R. X. (2017). Reconstruction of ocean's interior from observed sea surface information. *Journal of Geophysical Research: Oceans*, *122*(2), 1042–1056. https://doi.org/10.1002/2016jc011927

Liu, L., Peng, S., Wang, J., & Huang, R. X. (2014). Retrieving density and velocity fields of the ocean's interior from surface data. *Journal of Geophysical Research: Oceans*, *119*, 8512–8529. https://doi.org/10.1002/2014jc010221

Liu, L., Xue, H., & Sasaki, H. (2019). Reconstructing the ocean interior from high-resolution sea surface information. *Journal of Physical Oceanography*, *49*(12), 3245–3262. https://doi.org/10.1175/jpo-d-19-0118.1

Magalhães, F. C., Azevedo, J. L. L., & Oliveira, L. R. (2017). Energetics of eddy-mean flow interactions in the Brazil Current between 20°s and 36°s. *Journal of Geophysical Research: Oceans*, *122*(8), 6129–6146.

Martínez, J., Gabarró, C., Turiel, A., González-Gambau, V., Umbert, M., Hoareau, N., et al. (2021). Improved BEC SMOS Arctic Sea surface salinity product v3. 1. *Earth System Science Data Discussions*. https://doi.org/10.5194/essd-2021-334

McWilliams, J. C. (2016). Submesoscale currents in the ocean. *Proceedings of the Royal Society A: Mathematical, Physical & Engineering Sciences*, *472*(2189), 1–32. https://doi.org/10.1098/rspa.2016.0117

Morrow, R., Fu, L.-L., Ardhuin, F., Benkiran, M., Chapron, B., Cosme, E., & Zaron, E. D. (2019). Global observations of fine-scale ocean surface topography with the surface water and Ocean topography (SWOT) mission. *Frontier in Marine Science*, *6*(232), 1–19. https://doi.org/10.3389/fmars.2019.00232

Napolitano, D. C., da Silveira, I. C. A., Tandon, A., & Calil, P. H. R. (2021). Submesoscale phenomena due to the Brazil current crossing of the Vitória-Trindade Ridge. *Journal of Geophysical Research: Oceans*, *126*(1), 1–21. https://doi.org/10.1029/2020jc016731

Oliveira, F. S. C., & Polito, P. S. (2013). Characterization of westward propagating signals in the South Atlantic from altimeter and radiometer records. *Remote Sensing of Environment*, *134*, 367–376. https://doi.org/10.1016/j.rse.2013.03.019

Oliveira, L. R., Piola, A. R., Mata, M. M., & Soares, I. D. (2009). Brazil Current surface circulation and energetics observed from drifting buoys. *Journal of Geophysical Research*, *114*(C10). https://doi.org/10.1029/2008jc004900

Pegliasco, C., Chaigneau, A., & Morrow, R. (2015). Main eddy vertical structures observed in the four major Eastern Boundary Upwelling Systems. *Journal of Geophysical Research: Oceans*, *120*, 6008–6033. https://doi.org/10.1002/2015jc010950

Peterson, R. G., & Stramma, L. (1991). Upper-level circulation in the south Atlantic ocean. *Progress in Oceanography*, *26*, 1–73. https://doi.org/10.1016/0079-6611(91)90006-8

Phillips, N. A. (1954). Energy transformations and meridional circulations associated with simple baroclinic waves in a two-level, quasi-geostrophic model. *Tellus*, *6*(3), 274–286. https://doi.org/10.3402/tellusa.v6i3.8734

Polito, P. S., & Liu, W. T. (2003). Global characterization of Rossby waves at several spectral bands. *Journal of Geophysical Research*, *108*(C1), 1–18. https://doi.org/10.1029/2000jc000607

Polito, P. S., Sato, O. T., & Wainer, I. (2008). Height variability from the MIROC–IPCC model for the 20th century compared to that of the TOPEX/POSEIDON altimeter. *Ocean Modelling*, *24*(3–4), 73–91. https://doi.org/10.1016/j.ocemod.2008.04.007

Ponte, A. L. P., Klein Capet, X., Traon, P.-Y. L., Chapron, B., Lherminier, P., & Lherminier, P. (2013). Diagnosing surface mixed layer dynamics from high-resolution satellite observations: Numerical insights. *Journal of Physical Oceanography*, *43*(7), 1345–1355. https://doi.org/10.1175/jpo-d-12-0136.1

Qiu, B., Chen, S., Klein, P., Torres, H., Wang, J., Fu, L.-L., & Menemenlis, D. (2020). Reconstructing upper-ocean vertical velocity field from sea surface height in the presence of unbalanced motion. *Journal of Physical Oceanography*, *50*(1), 55–79. https://doi.org/10.1175/jpo-d-19-0172.1

Qiu, B., Chen, S., Klein, P., Ubelmann, C., Fu, L.-L., & Sasaki, H. (2016). Reconstructability of three-dimensional upper-ocean circulation from SWOT sea surface height measurements. *Journal of Physical Oceanography*, *46*(3), 947–963. https://doi.org/10.1175/jpo-d-15-0188.1

Richardson, P. L. (2007). Agulhas leakage into the Atlantic estimated with subsurface floats and surface drifters. *Deep Sea Research Part I: Oceanographic Research Papers*, *54*(8), 1361–1389. https://doi.org/10.1016/j.dsr.2007.04.010

Richman, J. G., Arbic, B. K., Shriver, J. F., Metzger, E. J., & Wallcraft, A. J. (2012). Inferring dynamics from the wavenumber spectra of an eddying global ocean model with embedded tides. *Journal of Geophysical Research*, *117*(C12012), 1–11. https://doi.org/10.1029/2012jc008364

Rocha, C. B., Chereskin, T. K., Gille, S. T., & Menemenlis, D. (2016). Seasonality of submesoscale dynamics in the Kuroshio extension. *Geophysical Research Letters*, *43*(11), 11304–11311. https://doi.org/10.1002/2016gl071349

Rocha, C. B., Gille, S. T., Chereskin, T. K., & Menemenlis, D. (2016). Mesoscale to submesoscale wavenumber spectra in Drake Passage. *Journal of Physical Oceanography*, *46*, 601–620. https://doi.org/10.1175/jpo-d-15-0087.1

Sasaki, H., & Klein, P. (2012). SSH wavenumber spectra in the North Pacific from a high-resolution realistic simulation. *Journal of Physical Oceanography*, *42*(7), 1233–1241. https://doi.org/10.1175/jpo-d-11-0180.1

Sasaki, H., Klein, P., Qiu, B., & Sasai, Y. (2014). Impact of oceanic-scale interactions on the seasonal modulation of ocean dynamics by the atmosphere. *Nature Communications*, *5*(5636), 1–8. https://doi.org/10.1038/ncomms6636

Silveira, I. C. A., Calado, L., Castro, B. M., Cirano, M., Lima, J. A. M., & Mascarenhas, A. S. (2004). On the baroclinic structure of the Brazil current–intermediate western boundary current system at 22–23°S. *Geophysical Research Letters*, *31*(14). https://doi.org/10.1029/2004gl020036

Silveira, I. C. A., de Miranda, L. B., & Brown, W. S. (1994). On the origins of the north Brazil current. *Journal of Geophysical Research*, *99*(C11), 22501–22512. https://doi.org/10.1029/94jc01776

Silveira, I. C. A., Lima, J. A. M., Schmidt, A. C. K., Ceccopieri, W., Sartori, A., Franscisco, C. P. F., & Fontes, R. F. C. (2008). Is the meander growth in the Brazil Current system off Southeast Brazil due to baroclinic instability? *Dynamics of Atmospheres and Oceans*, *45*(3), 187–207. https://doi.org/10.1016/j.dynatmoce.2008.01.002

Simoes-Sousa, I. T., Silveira, I. C. A., Tandon, A., Flierl, G. R., Ribeiro, C. H., & Martins, R. P. (2021). The Barreirinhas eddies: Stable energetic anticyclones in the near-equatorial South Atlantic. *Frontiers in Marine Science*, *8*, 11. https://doi.org/10.3389/fmars.2021.617011

Soutelino, R., Da Silveira, I., Gangopadhyay, A., & Miranda, J. (2011). Is the Brazil Current eddy-dominated to the north of 20°S? *Geophysical Research Letters*, *38*(3). https://doi.org/10.1029/2010gl046276

Stammer, D. (1997). Global characteristics of ocean variability estimated from regional TOPEX/POSEIDON altimeter measurements. *Journal of Physical Oceanography*, *27*, 1743–1769. https://doi.org/10.1175/1520-0485(1997)027<1743:gcoove>2.0.co;2

Tandon, A., & Garrett, C. (1995). Geostrophic adjustment and restratification of a mixed layer with horizontal gradients above a stratified layer. *Journal of Physical Oceanography*, *25*(10), 2229–2241. https://doi.org/10.1175/1520-0485(1995)025<2229:gaaroa>2.0.co;2

Thoppil, P. G., Richman, J. G., & Hogan, P. J. (2011). Energetics of a global ocean circulation model compared to observations. *Geophysical Research Letters*, *38*(15). https://doi.org/10.1029/2011gl048347

Turiel, A., Solé, J., Nieves, V., Ballabrera-Poy, J., & García-Ladona, E. (2008). Tracking oceanic currents by singularity analysis of Microwave Sea Surface Temperature images. *Remote Sensing of Environment*, *112*(5), 2246–2260. https://doi.org/10.1016/j.rse.2007.10.007

Uchida, T., Abernathey, R., & Smith, S. (2017). Seasonality of eddy kinetic energy in an eddy permitting global climate model. *Ocean Modelling*, *118*, 41–58. https://doi.org/10.1016/j.ocemod.2017.08.006

Vergara, O., Morrow, R., Pujol, I., Dibarboure, G., & Ubelmann, C. (2019). Revised global wave number spectra from recent altimeter observations. *Journal of Geophysical Research: Oceans*, *124*, 3523–3537. https://doi.org/10.1029/2018jc014844

Vinogradova, N., Lee, T., Boutin, J., Drushka, K., Fournier, S., Sabia, R., et al. (2019). Satellite salinity observing system: Recent discoveries and the way forward. *Frontiers in Marine Science*, *6*, 243. https://doi.org/10.3389/fmars.2019.00243

Wang, D., Flagg, C. N., Donohue, K., & Rossby, H. T. (2010). Wavenumber spectrum in the Gulf stream from shipboard ADCP observations and comparison with altimetry measurements. *Journal of Physical Oceanography*, *40*, 840–844. https://doi.org/10.1175/2009jpo4330.1

Wang, J., Flierl, G. R., LaCasce, J. H., McClean, J. L., & Mahadevan, A. (2013). Reconstructing the ocean's interior from surface data. *Journal of Physical Oceanography*, *43*, 1611–1626. https://doi.org/10.1175/jpo-d-12-0204.1

Wang, S., Quiao, F., Dai, D., & Zhou, X. (2019). Anisotropy of the sea surface height wavenumber spectrum from altimetry observations. *Scientific Reports*, *9*(1), 1–10. https://doi.org/10.1038/s41598-019-52328-w

Wunsch, C. (1997). The vertical partition of oceanic horizontal kinetic energy. *Journal of Physical Oceanography*, *27*, 1770–1794. https://doi.org/10.1175/1520-0485(1997)027<1770:tvpooh>2.0.co;2

Wunsch, C., & Stammer, D. (1995). The global frequency-wavenumber spectrum of oceanic variability estimated from TOPEX/POSEIDON altimeter measurements. *Journal of Geophysical Research*, *100*, 24895–24910. https://doi.org/10.1029/95jc01783

Xu, Y., & Fu, L. (2012). The effects of altimeter instrument noise on the estimation of the wavenumber spectrum of sea surface height. *Journal of Physical Oceanography*, *42*, 2229–2233. https://doi.org/10.1175/jpo-d-12-0106.1

Yan, H., Wang, H., Zhang, R., Chen, J., Bao, S., & Wang, G. (2020). A dynamical-statistical approach to retrieve the ocean interior structure from surface data: SQG-mEOF-R. *Journal of Geophysical Research: Oceans*, *125*(2), 1–15. https://doi.org/10.1029/2019jc015840